CHALMERS

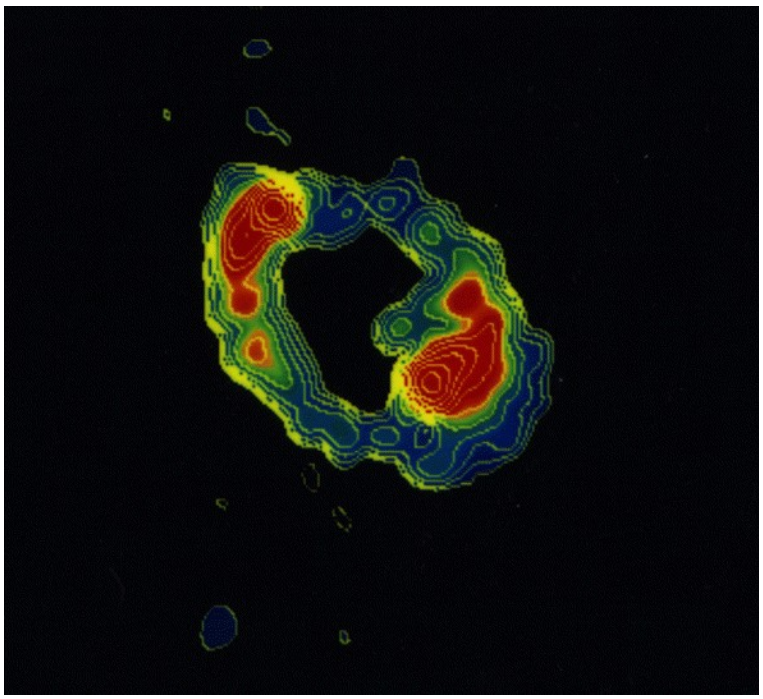

Modelling the Gravitationally Lensed Quasar PKS 1830-211

Master of Science Thesis in Physics and Astronomy

SARRVESH SEETHAPURAM SRIDHAR
Supervisors: Cathy Horellou and Sébastien Muller

Department of Earth and Space Sciences
Radio Astronomy and Astrophysics Group
CHALMERS UNIVERSITY OF TECHNOLOGY
Göteborg, Sweden, 2013

Thesis for the Degree of Master of Science in Physics and Astronomy

Modelling the Gravitationally Lensed Quasar PKS 1830-211

Sarrvesh Seethapuram Sridhar

Department of Earth and Space Sciences
CHALMERS UNIVERSITY OF TECHNOLOGY
Göteborg, Sweden 2013

Modelling the Gravitationally Lensed Quasar PKS 1830-211
Sarrvesh Seethapuram Sridhar

Thesis for the Degree of Master of Science in Physics and Astronomy

FRT 20xx:xx

Department of Earth and Space Sciences
CHALMERS UNIVERSITY OF TECHNOLOGY
SE-412 96 Göteborg
Sweden www.chalmers.se Tel. +46-(0)31 772 1000

Cover: 5 GHz MERLIN image of the radio Einstein ring towards PKS1830-211 (Patnaik *et al.*, 1993).

Printed by Reproservice
Göteborg, Sweden 2013

Modelling the Gravitationally Lensed Quasar PKS 1830-211

Sarrvesh Seethapuram Sridhar
Department of Earth and Space Sciences, Chalmers University of Technology

Abstract
The two lines of sight towards the gravitationally lensed quasar PKS 1830-211 have been used as a probe for a number of cosmological parameters like the temperature of the cosmic microwave background, variations in the fundamental constants, and the Hubble constant. Apart from being used as a cosmological probe, this gravitational lens system also offers a unique opportunity to study both the interstellar medium of lens galaxy and the radio jet of the background quasar. Although numerous high resolution observations have been performed towards the source quasar, there is no one single lens model that can account for all the observed characteristics of this system. As a first step towards achieving a unified model for both the background source and the lens galaxy, in this thesis, we have built a refined lens model using high resolution observations performed over the last decade. Using the new lens model, we estimate a value for the Hubble constant ($H_0 = 76 \pm 28$ km/s/Mpc). Though the uncertainty of H_0 is large, we found that it scales linearly with the uncertainty on the lens position and better constraints on the lens position through future observation could improve our H_0 estimate. We have also discussed several new methods – both observational and theoretical – with which the refined lens model can be greatly improved.

Keywords: *(Galaxies:)* quasars: individual: PKS 1830-211 – Gravitational lensing – *(Cosmology:)* cosmological parameters

"We are joined in a search for understanding, not grades."
– P. J. E. Peebles, Principles of Physical Cosmology.

Acknowledgements

First and foremost, I wish to thank my supervisors Cathy Horellou and Sébastien Muller for their tremendous support over the last six months. I am greatly indebted to a lot of people both in India and in Sweden for helping me switch my career from being a software engineer to an astronomer.

Last but not the least, this research has made use of NASA's Astrophysics Data System Bibliographic Services. This research has also made use of SAOImage DS9, developed by Smithsonian Astrophysical Observatory. I would also like to thank Dr. Charles Keeton (Rutgers University) for his timely responses regarding my queries related to the GRAVLENS software package.

Göteborg, August 2013
Sarrvesh S. Sridhar

Contents

Chapter 1

Introduction

Gravitational lensing is the bending or deflection of light from a source due to the presence of an arbitrary distribution of mass along its path. A schematic representation of gravitational lensing is shown in figure 1.1. The figure shows the deflection of light rays from a background galaxy by a galaxy cluster present in-between the source galaxy and the observer. The picture also shows that certain light rays (shown in orange) though follow different paths tend to converge at a specific location and the observer at that particular location will see two different images of a single background source. In the image, if the observer happens to be in the path of other light rays (which are shown in white), the observer will see a single, distorted image of the background source.

Though the relativistic formalism for gravitational lensing was presented in the beginning of the previous century (Chwolson, 1924; Einstein, 1936), the first gravitational lens was discovered almost half a century later (Walsh *et al.*, 1979). However, even before the discovery of the first gravitational lens, Refsdal (1964) predicted that gravitational lenses could in principle be used to determine the value of Hubble constant (H_0) and masses of galaxies. If the background source being lensed happens to be intrinsically variable, images of the background source produced by the lens will exhibit a time delay with respect to one another. If the time delay between the lensed images can be measured precisely, and if one has a model for the gravitational lens, these two can be combined to estimate the value of H_0 (see chapter 2 for a review of the mathematical theory of gravitational lensing). Eventhough being conceptually simple, determining a precise value of H_0 using gravitational lenses over the years has proven to be challenging due to uncertainties associated with the lens model.

A robust model that overcomes the above mentioned uncertainties related to lens modelling can have several other useful consequences apart from having a precise estimate for the value of H_0. For example, Vegetti *et al.* (2012) modelled the lens JVAS B1938+666 and detected the presence of a dwarf satellite galaxy near the primary lens. Such systematic studies of a number of gravitational lenses could shed light on the "missing satellite problem" associated with the Cold Dark Matter (CDM) scenario for cosmological structure formation. Instead of being a stand-alone probe, gravitational lenses can also be used in combination with other cosmological probes such as galaxy clustering and the integrated Sachs-Wolfe effect to study cosmic gravity (see for example Jain and Khoury, 2010; Cabré *et al.*, 2012).

The uncertainties associated with the lens modelling procedure can be overcome either by analysing a statistically large ensemble of gravitational lenses to estimate the value of H_0 or by studying individual lenses in great detail in order to account for possible sources of error in the modelling procedure. With the latter point in mind, we have chosen a single gravitational lens as the subject for this study. The source studied in this thesis – PKS 1830-211 – is a gravitationally lensed quasar and is interesting not only due to gravitational lensing but also due to its uses as other cosmological probes. A brief account of its uses as a cosmological probe and why a robust lens model for this system is required are presented

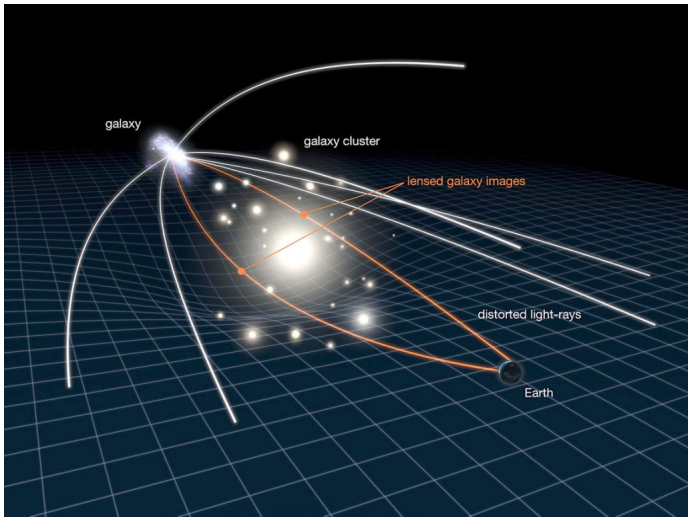

Figure 1.1: A typical gravitational lens. (Image: NASA/ESA)

in chapter 3. In chapter 4, we first review some of the recent lens modelling attempts for PKS 1830-211 before presenting our refined lens model for this system. We finally conclude by suggesting observations and modelling techniques that can be used to improve the lens model presented in this study.

Throughout this work, we assume a flat ΛCDM cosmology with $\Omega_m = 0.279$, $\Omega_\Lambda = 0.721$ (Hinshaw *et al.*, 2012) and $H_0 = 100h$ km/s/Mpc unless otherwise stated.

Chapter 2

Gravitational lensing[1]

This chapter deals with the theory of gravitational lensing where relevant mathematics is introduced in section 2.1 and in section 2.2 we review some of the commonly used mass distibutions for modelling spiral galaxies. In a realistic lensing scenario, the equations governing the lens "mapping" cannot be solved analytically and hence require numerical recipes. In section 2.3.1 we briefly review the commonly used numerical procedure that is used to solve the lens equation.

2.1 Lensing formalism

2.1.1 Lens equation

The theory of General Relativity predicts that a light ray passing close to a gravitating object gets deflected from its original path. If the ray impact parameter ξ – defined as the shortest distance between the center of mass of the gravitating object and the light ray – is smaller than the Schwarzschild radius R_S of the gravitating object, then the deflection angle $\hat{\boldsymbol{\alpha}}$ can be written as

$$\hat{\boldsymbol{\alpha}} = \frac{4GM}{c^2\xi} \tag{2.1}$$

if $\xi \ll R_S$ where $R_S = 2GMc^{-2}$. In the above equation, M is the mass of the gravitating object, G is the gravitational constant and c is the velocity of light. It is easy to see that the equations for deflection angle predicted by General Relativity and Newton's law of gravity differ by a factor of 2.

The assumption $\xi \ll R_S$ implies that the deflection angle $\hat{\boldsymbol{\alpha}} \ll 1$ and this allows one to denote the total deflection angle due to an ensemble of mass distribution as the sum of the deflection angles due to the individual mass elements present in that ensemble.

Thus equation 2.1 becomes

$$\hat{\boldsymbol{\alpha}} = \frac{4G}{c^2} \int d^2\xi \int dr_3' \rho(\xi_1', \xi_2', r_3') \frac{\boldsymbol{\xi} - \boldsymbol{\xi'}}{|\boldsymbol{\xi} - \boldsymbol{\xi'}|^2}. \tag{2.2}$$

The surface mass density is defined as

$$\Sigma(\boldsymbol{\xi}) = \int dr_3 \rho(\xi_1, \xi_2, r_3) \tag{2.3}$$

where r_3 is the component along the line of sight.

Employing such a definition, the deflection angle can then be re-written as

[1] This chapter relies heavily on Schneider *et al.* (2006).

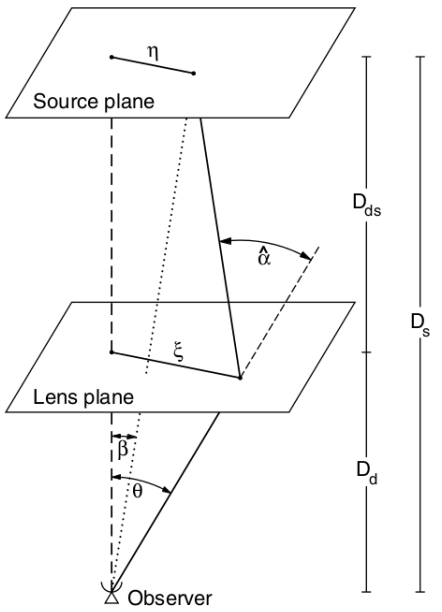

Figure 2.1: Sketch of a typical gravitational lens system. Image taken from Schneider *et al.* (2006).

$$\hat{\boldsymbol{\alpha}} = \frac{4G}{c^2} \int d^2\xi' \Sigma(\boldsymbol{\xi'}) \frac{\boldsymbol{\xi} - \boldsymbol{\xi'}}{|\boldsymbol{\xi} - \boldsymbol{\xi'}|^2}. \tag{2.4}$$

Now, consider a typical gravitational lens system as the one shown in figure 2.1. Let D_d, D_s and D_{ds} be the lens-to-observer, source-to-observer and lens-to-source distances respectively. In all astrophysically significant cases, the above mentioned distances are much larger than the radial sizes of the lens and the source, and hence both the lens and the source can be approximated to lie on planes perpendicular to the line of sight. The thick broken line running perpendicular to both the lens and the source plane is called the "optical axis" and is used as a reference for identifying the positions of the unlensed source and the observed image. A ray of light originating from the source plane, with a position vector $\boldsymbol{\eta}$, passes through the lens plane at a point with a position vector $\boldsymbol{\xi}$ and is deflected from its original path by an angle $\hat{\boldsymbol{\alpha}}$.

As stated earlier, the above mentioned definition for the deflection angle $\hat{\alpha}$ is valid only for the limit $\xi \gg R_s$ which corresponds to $\hat{\alpha} \ll 1$. For small values of $\hat{\alpha}$, the lens equation can be read of from the figure 2.1 using the small angle approximation as

$$\boldsymbol{\eta} = \frac{D_s}{D_d}\boldsymbol{\xi} - D_{ds}\hat{\boldsymbol{\alpha}}(\boldsymbol{\xi}) \tag{2.5}$$

In terms of the angular coordinates $\boldsymbol{\eta} = D_{ds}\boldsymbol{\beta}$ and $\boldsymbol{\xi} = D_d\boldsymbol{\theta}$, equation 2.5 can be written as

$$\boldsymbol{\beta} = \boldsymbol{\theta} - \frac{D_{ds}}{D_s}\hat{\boldsymbol{\alpha}}(D_d\boldsymbol{\theta}) \tag{2.6}$$

From equation 2.4, we have

$$\hat{\boldsymbol{\alpha}}(\boldsymbol{\xi}) = \frac{4G}{c^2} \int d^2\boldsymbol{\xi'} \Sigma(\boldsymbol{\xi'}) \frac{\boldsymbol{\xi} - \boldsymbol{\xi'}}{|\boldsymbol{\xi} - \boldsymbol{\xi'}|^2} \tag{2.7}$$

$$\Rightarrow \hat{\boldsymbol{\alpha}}(\boldsymbol{\theta}) = \frac{4G}{c^2} D_d \int d^2\boldsymbol{\theta'} \Sigma(\boldsymbol{\theta'}) \frac{\boldsymbol{\theta} - \boldsymbol{\theta'}}{|\boldsymbol{\theta} - \boldsymbol{\theta'}|^2} \tag{2.8}$$

Substituting this in equation 2.6, we rewrite the lens equation in terms of scaled deflection angle $\boldsymbol{\alpha}(\boldsymbol{\theta})$ as

$$\boldsymbol{\beta} = \boldsymbol{\theta} - \boldsymbol{\alpha}(\boldsymbol{\theta}) \tag{2.9}$$

where the scaled deflection angle formulated using the dimensionless surface mass density or convergence $\kappa(\boldsymbol{\theta})$ as

$$\boldsymbol{\alpha}(\boldsymbol{\theta}) = \frac{1}{\pi} \int d^2\boldsymbol{\theta'} \kappa(\boldsymbol{\theta'}) \frac{\boldsymbol{\theta} - \boldsymbol{\theta'}}{|\boldsymbol{\theta} - \boldsymbol{\theta'}|^2} \tag{2.10}$$

such that

$$\kappa(\boldsymbol{\theta}) \equiv \frac{\Sigma(D_d\boldsymbol{\theta})}{\Sigma_{cr}} \tag{2.11}$$

and

$$\Sigma_{cr} \equiv \frac{c^2}{4\pi G} \frac{D_s}{D_d D_{ds}}. \tag{2.12}$$

In equations 2.11 and 2.12, Σ_{cr} is the critical surface mass density which depends only on the distances involved in defining the lens model. It can be seen that the equation 2.9 is simply a mapping between the position on the source plane $\boldsymbol{\xi}$ to the position on the image plane $\boldsymbol{\theta}$.

2.1.2 Image magnification

Since light is deflected differentially by the lens, the shapes of the images produced due to lensing will differ significantly from that of the source. If the source under consideration is much smaller than the scale on which the lens properties change, then the distortion of the images can be described using the Jacobian matrix

$$\boldsymbol{A}(\boldsymbol{\theta}) = \frac{\partial \boldsymbol{\beta}}{\partial \boldsymbol{\theta}} = \left(\delta_{ij} - \frac{\partial^2 \psi(\boldsymbol{\theta})}{\partial\theta_i \partial\theta_j} \right) = \begin{pmatrix} 1 - \kappa - \gamma_1 & -\gamma_2 \\ -\gamma_2 & 1 - \kappa + \gamma_1 \end{pmatrix} \tag{2.13}$$

where γ_1 and γ_2 are the components of shear $\gamma = \gamma_1 + i\gamma_2$ defined as

$$\gamma_1 = \frac{1}{2}(\psi_{,11} - \psi_{,22}) \quad ; \quad \gamma_2 = \psi_{,12} \tag{2.14}$$

such that

$$\psi_{,ij}(\theta) = \frac{\partial^2 \psi(\theta)}{\partial\theta_i \partial\theta_j} \tag{2.15}$$

and ψ is the deflection potential defined as

$$\psi(\boldsymbol{\theta}) = \frac{1}{\pi} \int_{\mathbb{R}^2} d^2\theta' \kappa(\boldsymbol{\theta'}) \ln |\boldsymbol{\theta} - \boldsymbol{\theta'}|. \tag{2.16}$$

Furthermore, the deflection potential ψ is related to the convergence κ through the two-dimensional Poisson equation as

$$\nabla^2 \psi = 2\kappa. \tag{2.17}$$

The magnification μ of the lensed images, or the ratio between the flux observed from the images to the flux from the unlensed source, can be computed from the distortion matrix $\boldsymbol{A}$ as

$$\mu = \frac{1}{det\boldsymbol{A}} = \frac{1}{(1-\kappa)^2 - |\gamma|^2} \tag{2.18}$$

The sign and the magnitude of μ, at each point on the image plane, can have important consequences for images formed at those points. Magnification μ, as defined in equation (2.18), can have both positive and negative values. The sign on μ is called the parity of an image. If an image has negative parity, the observed image will be mirror-symmetric with respect to the source. Since the flux of the source is unknown in a typical lensing system, the magnification μ, as defined above, is not an observable and hence the practice is to use the ratio of magnification of different images to constrain the lens model.

For any given lens model, the value of magnification μ can diverge at certain points on the image plane. These points are called *critical points* and the closed curves connecting the critical points on the image plane are called *critical lines* which form *caustics* when mapped onto the source plane. It is important to realize that while the critical lines divide the image plane into regions with positive and negative parity, the corresponding caustics divide the source plane into regions capable of producing different numbers of images.

When a gravitational lens is used a natural telescope to study sources located at higher redshifts, having a magnification map for a given mass distribution could be quite useful. For example, consider a scenario where sub-millimetre galaxies at higher redshifts are lensed or magnified by an intervening galaxy cluster. If one possesses a robust mass model for the galaxy cluster, this information can be used to generate the magnification maps for the cluster. By coinciding the generated magnification map with the observational data, one can simply read off the amount by which the background galaxies have been magnified which can then be used to extract the intrinsic brightness of those galaxies.

A MATLAB code was written to generate the above mentioned magnification maps and we checked the correctness of the code by comparing our results with the maps published in Schneider and Weiss (1986). Figures 2.2 and 2.3 show the comparison between the simulated and the published maps for a 2-point mass lens. The MATLAB code to simulate the magnification maps for a 2-point mass lens and a 2-SIS lens are included in appendices G and H respectively. The code can be used to generate magnification maps for any distribution of mass with very little modification.

2.1.3 Number of images

The total number of images produced by a given lens model depends on the position of the source with respect to the cautic lines on the source plane. For example, consider a simple lens model consisting of a Singular Isothermal Sphere (SIS) as the lens whose lens parameters are given in table 2.1 (See section §2.2 for more information on the SIS lens model). Figure 2.4 shows the position of three sources with respect to the caustics on the source plane and figure 2.5 contains images corresponding to each of the displayed source positions. It is easy to note that the outer caustic determines whether the source gets multiply imaged or not. The lens model produces multiple images for all sources residing inside the outer caustic whereas it produces a single image for sources lying outside the outer caustic. When the source is present inside both the caustics, as depicted by a red-coloured plus, the source gets lensed into five different images and when the source is present inbetween both the caustics, as shown using a black-coloured cross, it gets lensed into three images. It can also be seen that the third and the fifth image for the latter cases form very close to the center of the lens and is highly demagnified making it very difficult to observe in real lensing scenarios.

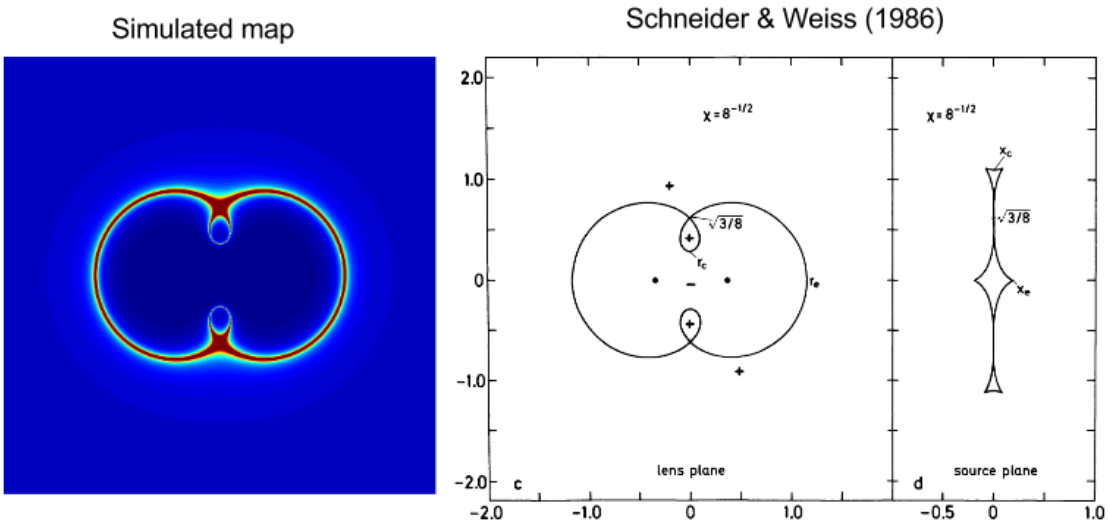

Figure 2.2: *Left:* Simulated magnification map for a two point source placed at 0".707 apart. *Right:* Magnification map published in Schneider and Weiss (1986) for the same set up.

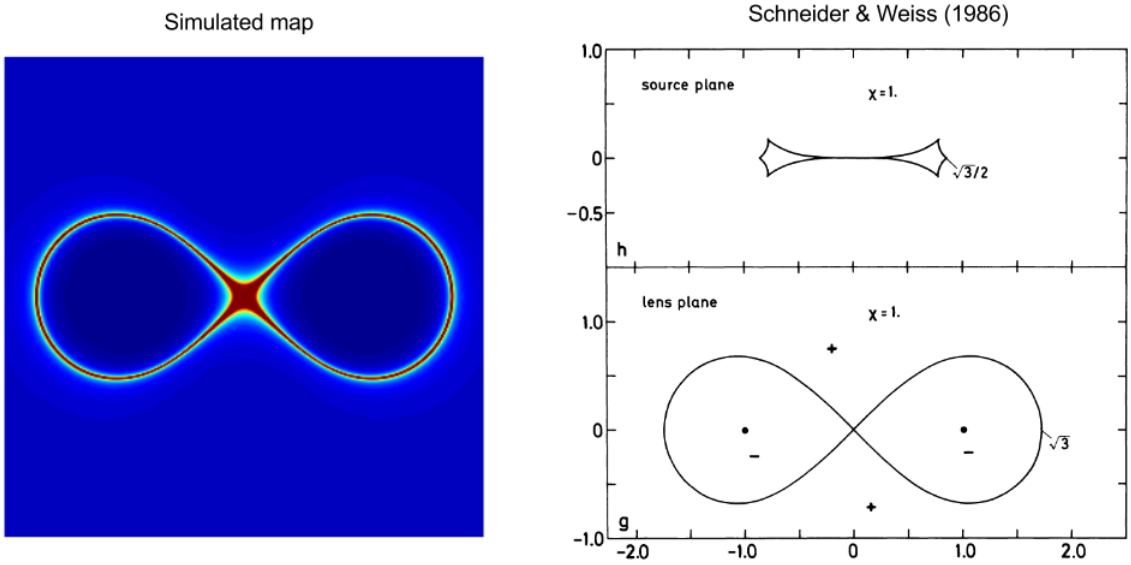

Figure 2.3: *Left:* Simulated magnification map for a two point source placed at 1" apart. *Right:* Magnification map published in Schneider and Weiss (1986) for the same set up.

Table 2.1: SIS lens model parameters for figures 2.4 and 2.5. The redshifts are those of the PKS 1830-211 system.

Parameter	**Value**
Source redshift	2.507
Lens redshift	0.886
Lens ellipticity, e	0.5
Position angle of the lens	0 °
1-D velocity dispersion of the lens	188 km/s

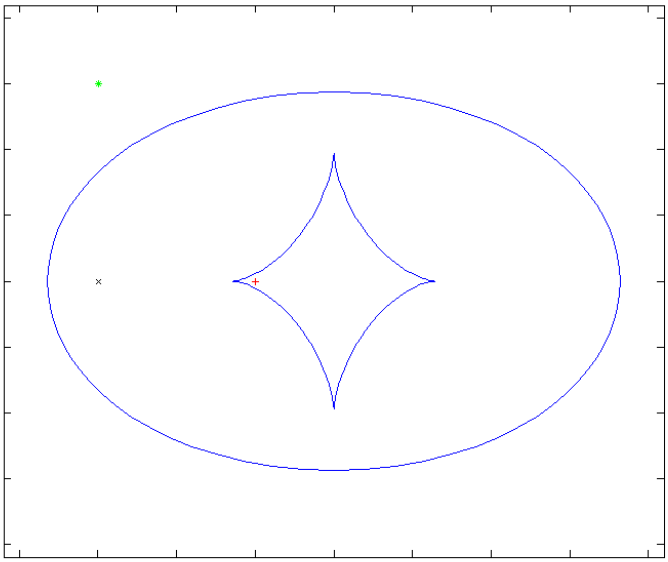

Figure 2.4: Position of three sources on the source plane

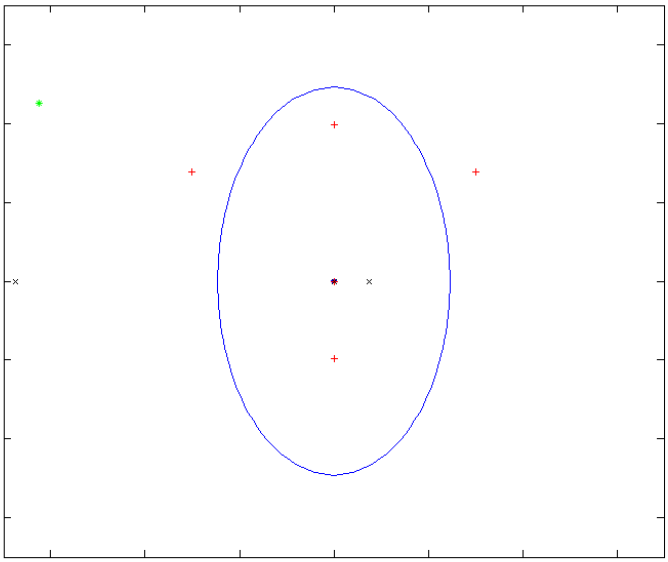

Figure 2.5: Images corresponding to each source position in fig. 2.4

2.1.4 Time delay between images

In the case of gravitational lenses producing multiple images of the background source, the wavefront travelling along each of these lines of sight experience a time delay with respect to the "no-lensing" scenario and with respect to each other. Time delay induced between any two images in lensing is due to two physical effects: (i) since the two images under consideration are not always equidistant from the center of mass of the lens mass distribution, a small time delay is induced due to general relativistic effects, and (ii) as the lines of sight through these two images are different, light travelling through these images have different light-travel-time.

For a source located at angular position $\boldsymbol{\beta}$ on the source plane, an image at angular position $\boldsymbol{\theta}$ experiences a time delay $t\left(\boldsymbol{\theta},\boldsymbol{\beta}\right)$ with respect to the "no lensing" scenario given as

$$t\left(\boldsymbol{\theta},\boldsymbol{\beta}\right)=\frac{D_{\Delta t}}{c}\left[\frac{\left(\boldsymbol{\theta}-\boldsymbol{\beta}\right)^{2}}{2}-\psi\left(\boldsymbol{\theta}\right)\right], \tag{2.19}$$

where c is the velocity of light, $D_{\Delta t}$ is the time delay distance and $\psi(\boldsymbol{\theta})$ is the deflection (or lens) potential. The time delay distance is related to the angular diameter distance between the lens and observer (D_d), source and lens (D_{ds}), and source and observer (D_s) as

$$D_{\Delta t}\equiv\left(1+z_{d}\right)\frac{D_{d}D_{s}}{D_{ds}}. \tag{2.20}$$

Now, using equation (2.19), time delay between two images Δt_{ij} with angular positions $\boldsymbol{\theta}_i$ and $\boldsymbol{\theta}_j$ is given as

$$\Delta t_{ij}=\frac{D_{\Delta t}}{c}\left[\frac{\left(\boldsymbol{\theta}_{i}-\boldsymbol{\beta}\right)^{2}}{2}-\psi\left(\boldsymbol{\theta}_{i}\right)-\frac{\left(\boldsymbol{\theta}_{j}-\boldsymbol{\beta}\right)^{2}}{2}+\psi\left(\boldsymbol{\theta}_{j}\right)\right]. \tag{2.21}$$

By measuring the time delay between multiple images through long term monitoring and by modelling the lens potential with an appropriate mass distribution, the time delay distance $D_{\Delta t}$ can be computed. Since $D_{\Delta t}$ involves just the redshift and the angular diameter distances, it can be used to measure the value of the Hubble constant H_0 for a given set of cosmological parameters. As a special case, for isolated gravitational lenses with an isothermal mass distribution whose potential is of the form

$$\phi=r\mathcal{F}(\theta) \tag{2.22}$$

where $\mathcal{F}(\theta)$ is some arbitrary function of θ, Witt *et al.* (2000) have shown that time delay between two images can be expressed as

$$\Delta t_{i,j}=\frac{D_{d}D_{s}}{D_{ds}}\frac{\left(1+z_{d}\right)}{2c}(r_{j}^{2}-r_{i}^{2}) \tag{2.23}$$

where r_i is the distance between the center of the lens and the i^{th} image, z_d is the lens redshift. The essence of the above equation is that for a lens whose mass distribution can be approximated as an isothermal mass distribution, the time delay between two images does not depend on the exact mass profile used to model the lens.

2.2 Simple Mass models

2.2.1 Singular Isothermal Sphere (SIS)

One of the simplest mass models that can be solved analytically is that of the singular isothermal sphere. Its surface mass density is given by the equation

$$\Sigma(\boldsymbol{\xi})=\frac{\sigma_{v}^{2}}{2G}\xi^{-1} \tag{2.24}$$

where σ_v is the line of sight velocity dispersion of the particles in the halo that is described using the SIS profile and $\boldsymbol{\xi}$ is given in polar coordinates $(\xi\cos\phi, \xi\sin\phi)$. Convergence κ can then be written as

$$\kappa \equiv \frac{\Sigma}{\Sigma_{cr}} = 2\pi \left(\frac{\sigma_v}{c}\right)^2 \frac{D_d D_{ds}}{D_s} \xi^{-1} \tag{2.25}$$

where Σ_{cr} is defined in equation (2.12). If the Einstein radius θ_E is defined as

$$\theta_E = 4\pi \left(\frac{\sigma_v}{c}\right)^2 \frac{D_d D_{ds}}{D_s}, \tag{2.26}$$

equation (2.25) can be rewritten as

$$\kappa(\xi) = \frac{\theta_E}{2\xi}. \tag{2.27}$$

Making a change of variable defined as $x \equiv \xi/\theta_E$, convergence κ and deflection angle α can be written as

$$\kappa(x) = \frac{1}{2x} \quad ; \quad \alpha(x) = \frac{x}{|x|}. \tag{2.28}$$

Thus the lens equation for a singular isothermal sphere can be written as

$$\boldsymbol{y} = \boldsymbol{x} - \frac{\boldsymbol{x}}{|\boldsymbol{x}|} \tag{2.29}$$

where the angular position of the source on the source plane η is defined as $\boldsymbol{\eta} \equiv \boldsymbol{y}\theta_E$. For an image appearing at position x, its magnification μ can be computed using equation (2.18) as

$$\mu = \frac{|x|}{|x| - 1}. \tag{2.30}$$

Due to its simple analytical nature and spherical symmetry, the SIS mass distribution has been used extensively to model gravitational lenses (Turner *et al.*, 1984). However, modelling realistic gravitational lenses require more generalized mass distributions which are discussed in the following sections.

2.2.2 Singular Isothermal Ellipsoid (SIE)

One straightforward way to achieve a complex mass distribution is to generalize the singular isothermal sphere discussed in section §2.2.1. By replacing the radial coordinate ξ using an ellipsoidal coordinate ζ, it is possible to derive an isothermal profile with an ellipsoidal distribution called singular isothermal ellipsoid. In this section, a brief review of the equations concerning the SIE profile is presented. For a complete analysis of the SIE mass distribution, the reader is referred to Kormann *et al.* (1994).

Replacing ξ in equation (2.24) with ζ, the surface mass distribution of an SIE lens is

$$\Sigma = \frac{\sqrt{f}\,\sigma_v^2}{2G}\frac{1}{\zeta} = \frac{\sqrt{f}\,\sigma_v^2}{2G}\frac{1}{\sqrt{\xi_1^2 + f^2\xi_2^2}} \tag{2.31}$$

where f is the axis ratio whose value ranges within the interval $0 \leq f \leq 1$. Using the same definition of the Einstein radius made in equation (2.26), convergence κ for SIE can be written as

$$\kappa = \frac{\sqrt{f}}{2b} \tag{2.32}$$

such that

$$b \equiv \frac{\zeta}{\theta_E} = \sqrt{x_1^2 + f^2 x_2^2} \tag{2.33}$$

where $x_1 \equiv \xi_1/\theta_E$ and $x_2 \equiv \xi_2/\theta_E$. Using equations (2.17) and (2.32), the lensing potential ψ is

$$\psi(x,\phi) = \frac{\sqrt{f}x}{f'}\left[\sin\phi \arcsin\left(f'\sin\phi\right) + \cos\phi \sinh^{-1}\left(\frac{f'}{f}\cos\phi\right)\right] \tag{2.34}$$

where $f' = \sqrt{1-f^2}$.Computing the deflection angle using the formula $\alpha = \nabla\psi$, the lens equation can be written as

$$\boldsymbol{y} = \boldsymbol{x} - \frac{\sqrt{f}}{f'}\left[\sinh^{-1}\left(\frac{f'}{f}\cos\phi\right)e_1 + \arcsin\left(f'\sin\phi\right)e_2\right] \tag{2.35}$$

where e_1 and e_2 are unit vectors pointing along the directions x_1 and x_2.

One of the most important complications reached by generalising the simple equations of a singular isothermal sphere is that equation (2.35) cannot be solved analytically to find the lens position x for a given source position y thus requiring numerical root finding algorithms. An accurate and fast procedure to solving this equation is presented in Barkana (1998).

2.2.3 Navarro Frenk White (NFW) profile

Though the previous models discussed so far were first formulated on the basis of simplicity and not with any formal physical backing, the NFW profile was formulated based on results from N-body simulations (Navarro *et al.*, 1997). As in the case of SIE, only the relevant lensing equations are given in this section. For an in-depth treatment of lensing due to the NFW profile can be found in Bartelmann (1996) and Golse and Kneib (2002). The three dimensional density distribution ρ for a spherical NFW profile is

$$\rho(r) = \frac{\rho_c}{(r/r_s)\left(1+r/r_s\right)^2} \tag{2.36}$$

where ρ_c and r_s are characteristic density and scale radius respectively. The projected surface mass density in terms of dimensionless coordinates $\boldsymbol{x} = (x_1, x_2) = \boldsymbol{r}/r_s$ is (Golse and Kneib, 2002)

$$\Sigma(x) = \frac{2\rho_c r_s}{f}(x) \tag{2.37}$$

with

$$f(x) = \begin{cases} \frac{1}{x^2-1}\left(1 - \frac{1}{\sqrt{x^2-1}}\cos^{-1}\frac{1}{x}\right) & (x>1) \\ \frac{1}{3} & (x=0) \\ \frac{1}{x^2-1}\left(1 - \frac{1}{\sqrt{1-x^2}}\cosh^{-1}\frac{1}{x}\right) & (x<1)\,. \end{cases} \tag{2.38}$$

Convergence κ can be written using its standard definition as

$$\kappa(x) = \frac{\Sigma(x)}{\Sigma_c r} = 2\kappa_s f(x) \tag{2.39}$$

where $\kappa_s \equiv \rho_c r_s/\Sigma_{cr}$ and the deflection angle $\alpha(x)$ is

$$\boldsymbol{\alpha}(x) = 4\kappa_s \frac{\theta}{x^2} g(x)\, \boldsymbol{e}_x \tag{2.40}$$

where

$$g(x) = \begin{cases} \ln\frac{x}{2} + \frac{1}{\sqrt{1-x^2}}\cosh^{-1}\frac{1}{x} & (x<1) \\ 1 + \ln\frac{1}{2} & (x=1) \\ \ln\frac{x}{2} + \frac{1}{\sqrt{x^2-1}}\cos^{-1}\frac{1}{x} & (x>1) \end{cases} \tag{2.41}$$

and $\theta \equiv r/D_d$.

Among the two most commonly used models in gravitational lensing, the SIE mass distribution is generally used to represent galaxies whereas the NFW profile is used to model galaxy clusters.

2.2.4 Component-wise models for spiral galaxies

As discussed in the previous sections, though smooth mass distributions like SIE and NFW profiles have been used successfully in modelling gravitational lenses, numerous authors have argued recently that lens mass distribution should take into account small scale mass substructures $\left(\sim 10^9 M_\odot\right)$ in order to achieve a realistic lens model (Dalal and Kochanek, 2002). Following such a line of thought, a number of detailed lens models for spiral galaxies have been proposed by modelling each component of the spiral galaxy separately (Keeton and Kochanek, 1998; Koopmans *et al.*, 1998). The general practice is to use a three-component lens (halo-bulge-disk) for spiral galaxies and a two-component (halo and stars) mass model for elliptical galaxies.

In the case of spiral galaxies, both the halo and the bulge are modelled using an SIE mass distribution while the disk is modelled either as a flattened SIE or an exponential disk. Such complex modelling can be realised using simple equations due to the additive nature of gravitational lensing (i.e.) the total deflection angle at a given point due to a complex distribution of mass can be written as a linear sum of deflection produced by the individual components constituting the total mass distribution. However, increasing the complexity of the lens simultaneously increases the number of free model parameters which is a cause for concern while performing lens model fitting.

2.3 Numerical lensing

As stated before, one of the important goals for building a strong lens model is to study how the shape and the surface brightness distribution of an unlensed source is distorted by the presence of a mass situated close to the line of sight. This is achieved by inverting the lens equation (eq. 2.9) for the appropriate mass models to find the set of image positions $\boldsymbol{\beta}$ for a given source position $\boldsymbol{\theta}$. Though the lens equations derived in section §2.2 for simple mass models are relatively easy to solve, the problem becomes more complicated for a realistic mass distribution owing to the non-linearity of the equation. The equation is impossible to solve for an arbitrary mass model either analytically or numerically due to the unavailability of any generic numerical algorithm to find all the roots of a two dimensional equation (Press *et al.*, 1992). In order to overcome such a shortcoming, numerous techniques have been proposed over the years to perform the transformation from the source plane to the image. In section §2.3.1, we briefly review one such technique that is commonly used for solving the lens equation. For a thorough treatment of numerical lensing and for different imaging procedures for modelling extending sources, see chapter 10 in Schneider *et al.* (1992) and Kayser and Schramm (1988) respectively.

2.3.1 Tiling mechanism

The tiling method or the grid search method attempts to solve the problem of solving the lens equation by simply inverting equation 2.9. If we recall the physical interpretation of equation 2.9, each point on the source plane $\boldsymbol{\beta}$ is mapped to one or more points on the image plane $\boldsymbol{\theta}$. If the interpretation of the equation is inverted such that any given point $\boldsymbol{\theta}$ on the image plane is mapped to another point $\boldsymbol{\beta}$ on the source plane, then the problem at hand becomes much easier to solve.

The algorithm for solving the lens equation using the tiling mechanism is as follows: The first step is to grid the entire image plane with required grid resolution. Each of these tiles forming the grid on the image plane can be readily mapped onto the source plane using equation 2.9. Now, a source on the source plane will lie on at least one of the mapped tiles. By remapping the tile that covers the point source to the image plane, the corresponding image position can be identified. If more than one tile covers the point source on the source

plane, this results in two images whose positions would correspond to the positions occupied by those tiles on the image plane.

Since the tiles have a physical extent, the accuracy of the derived image positions will be limited by the grid resolution used to cover the image plane grid. The accuracy of the image positions can be improved significantly either by increasing the resolution of the image plane grid or by using any numerical root finder to refine the result based on the estimate provided by the tiling method.

Numerous software packages can be found in the literature that have been created to model different aspects of strong lensing. A systematic review of 12 such softwares can be found in Lefor *et al.* (2012). Throughout this thesis, lens modelling is done using the software package GRAVLENS. A brief introduction to the GRAVLENS software package and some of the relevant aspects of the package are reviewed in appendix B.

Chapter 3

Overview of PKS 1830-211

The gravitationally lensed blazar PKS 1830-211[1] was first identified as a single, bright source in the Parkes survey(Shimmins *et al.*, 1969). Although originally suspected to be a Phillips-Mutel type double (Phillips and Mutel, 1982), Pramesh Rao and Subrahmanyan (1988) suggested that the observed double structure with flat-spectrum cores was probably due to the gravitational lensing of a background compact radio source by a foreground galaxy. Using the twin epoch observations from Pramesh Rao and Subrahmanyan (1988) and new high resolution VLA observations at wavelengths λ = 6, 2 and 1.3 cm, Subrahmanyan *et al.* (1990) decomposed the north-east (NE) and the south-west (SW) components into a core-jet-knot structure and built the first lensing model to validate the interpretation of Pramesh Rao and Subrahmanyan (1988). Although the model was able to explain some of the observed source structure, it was prone to being unlikely due to the unknown redshifts of the lens and the source. The first strong evidence for the lensing scenario came in 1991 with the discovery of an elliptical ring connecting the two components by Jauncey *et al.* (1991) which was followed by extensive lens models replicating the observed Einstein ring and the two components (Kochanek and Narayan 1992;Nair *et al.* 1993).

All lens models built thus far, though being successful to a certain extent, were handicapped due to the unknown values of the source and lens redshifts. Though some of these lens models were able to estimate the time delay between the two images, the estimated values ranged between one single day and several tens of days (for example see Nair *et al.*, 1993). As the target object lies close to the Galactic plane ($b = -5^\circ.7$), searches for the optical counterpart was impossible due to Galactic dust extinction and hence most of the information came from the radio and mm observations. Absorption lines of 12 molecules were identified in the lensing galaxy by Wiklind and Combes (1996) and were used to derive the lens redshift. The determined lens redshift of $z = 0.89$ was later confirmed with X-ray absorption lines using ROSAT (Mathur and Nair, 1997) and HI absorption (Chengalur *et al.*, 1999). Based on the abundances of different molecular species at $z = 0.89$ and the relative velocity components between the two lines of sight, Wiklind and Combes (1996) predicted that the lens is most probably a near-face-on spiral galaxy. Koopmans and de Bruyn (2005) performed the first kinematic lens modelling of PKS 1830-211 by combining 21 cm HI observations with the underlying lens model. Instead of choosing a single lens position, Koopmans and de Bruyn (2005) considered several lens positions that have been reported in the literature and derived an inclination angle of $(17^\circ - 32^\circ)\pm 2^\circ$ for the HI disk, which is consistent with a near-face-on spiral lens. Lovell *et al.* (1996) reported a possible HI absorption at a redshift of $z = 0.19$ while Wiklind and Combes (1998) found no molecu-

[1] *Terminology:* Throughout the rest of this report, the term 'PKS 1830-211' when used without any qualifiers attached to it refers to the entire line of sight consisting of a spiral lens at z = 0.89 and a quasar at z=2.51. The lens is usually referred to as 'the lens towards PKS 1830-211' and the source as 'the background quasar'.

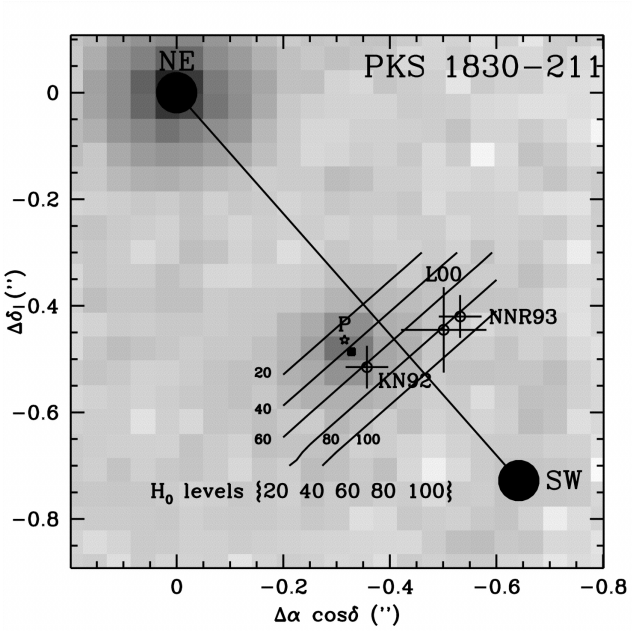

Figure 3.1: Lens positions used by different authors (Lehar *et al.* (2000), Nair *et al.* (1993) and Kochanek and Narayan (1992)) to model PKS 1830-211. The filled square is the lens position used by Winn *et al.*

lar absorption or emission at this redshift and also suggested that either the HI absorption at $z = 0.19$ could be reinterpreted as absorption of a heavier molecule at $z = 0.89$ or the second galaxy is located away from the line of sight towards the blazar causing no major contribution to the gravitational lensing.

Using a 13-month monitoring at 8.4 GHz and 15 GHz with the Very Large Array (VLA), van Ommen *et al.* (1995) estimated a time delay of 44 ± 9 days between the two images. However, based on an 18-month monitoring using the Australia Telescope Compact Array (ATCA), Lovell *et al.* (1998) reported a much lower time delay of 26^{+4}_{-5} days which was later confirmed by Wiklind and Combes (2001) who reported a time delay of 24^{+5}_{-4} days. Recently, Barnacka *et al.* (2011) derived a time delay of 27.1 ± 0.6 days using gamma-ray observations from Fermi-LAT.

Finally, the much awaited source redshift was measured to be $z = 2.51$ using the infrared spectrograph SOFI on ESO's New Technology Telescope (Lidman *et al.*, 1999) using the Hα and Hβ emission lines. Using the time delay of 26^{+4}_{-5} days between the two lensed images reported by (Lovell *et al.*, 1998), Lidman *et al.* (1999) estimated the value of Hubble constant as $H_0 = 76^{+15}_{-9}$ for $\Omega_m = 0.3$ assuming that the barycenter of the lens galaxy is very close to the center of the Einstein's ring. The large error bars in the derived value of the Hubble constant are due to the error bars in the measured time delay, but the uncertainty in the position of the lens galaxy will increase the error bars. Following this, in an attempt to determine the accurate position of the lens, numerous optical searches were performed. Lehar *et al.* (2000) were able to detect the lens galaxy but were unable to determine the exact lens positions. Using the same Hubble Space Telescope (HST) observation, Winn *et al.* (2002) and Courbin *et al.* (2002) reported two different lens position. Figure 3.1 shows various lens positions that have been used to model the gravitational lens towards PKS 1830-211.

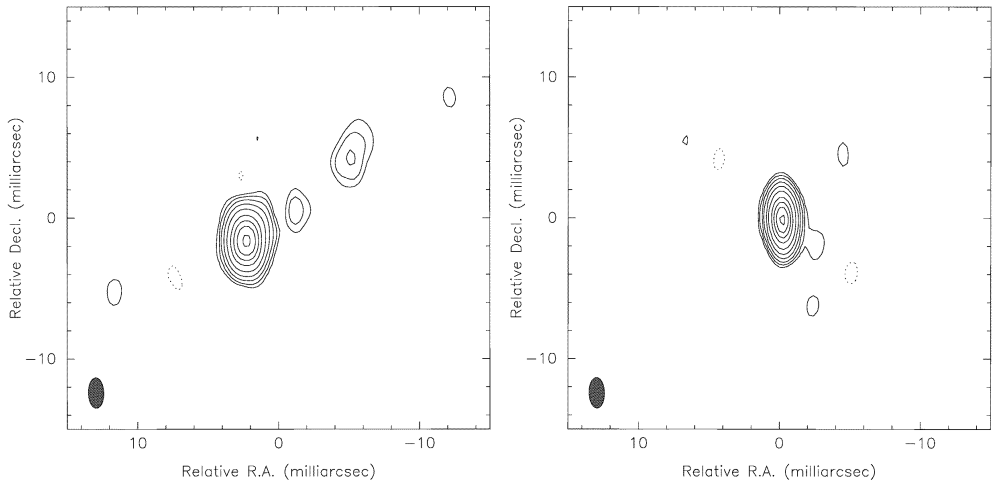

Figure 3.2: 22 GHz observations of the NE (left) and the SW (right) images of PKS 1830-211 (Jones *et al.*, 1996). Note that the two blobs visible near the 2 o'clock position in the NE image have no counterpart in the SW image.

3.1 Variations in the lensed radio cores

On the arc second scale, the two lensed images of PKS 1830-211 can be decomposed into two components: a flat-spectrum core and a diffuse jet that is large enough to form a pseudo Einstein ring (see *front cover*). On this scale, the two images are point-inverse symmetric and the knots in both the images are aligned in such a way that they are nearly perpendicular to the line joining the two bright cores.

On the milli-arc sec scale, a $\sim$ 12 mas jet is observed at 15 GHz (Garrett *et al.*, 1998) in the NE image which has no discernable counterpart in the SW image. The same feature is also observed at 8.4 GHz (Guirado *et al.*, 1999) and at 22 GHz (Jones *et al.*, 1996) (see figure 3.2). An inner knot is also seen at 43 GHz (Jin *et al.*, 2003) which appears to be lying on the same side of the core as the arc sec knot.

With multi-epoch VLBI observations over several months at 43 GHz, Jin *et al.* (2003) report that the angular separation between the two bright cores appears to shift by 10s-100s μas depending on the observed epoch. Figure 3.4 shows the change in the separation between the bright cores with respect to previous 43 GHz observations (denoted as '01' in the figure) published in Garrett *et al.* (1997). An initial attempt to explain the observed change in the relative positions of the imaged cores due to millilensing effects resulted in an under estimation of the observed deviation (Jin *et al.*, 2003). Also, based on the largest shift that appears between epoch 4 and 5 (see figure 3.4), Jin *et al.* (2003) estimated that the background blazar must exhibit relativistic beaming exceeding 10c.

Nair *et al.* (2005) try to interpret the variations seen by Jin *et al.* (2003) as events occuring due to the emissions of "plasmons" from the central core along a precessing jet. As plasmons are emitting along the quasar jet, the centroid of emission on the source plane shifts around which when lensed produces the observed changes in the separation between the two bright cores on the image plane. Based on the eight epoch observations from Jin *et al.* (2003), Nair *et al.* (2005) estimate a precessional period of $\approx$ 1.08 yr assuming the axis of precession is aligned along the line of sight. They also claim that these "plasmons" cannot be the projenitors of the $\sim$ 12 mas jet seen by Garrett *et al.* (1998).

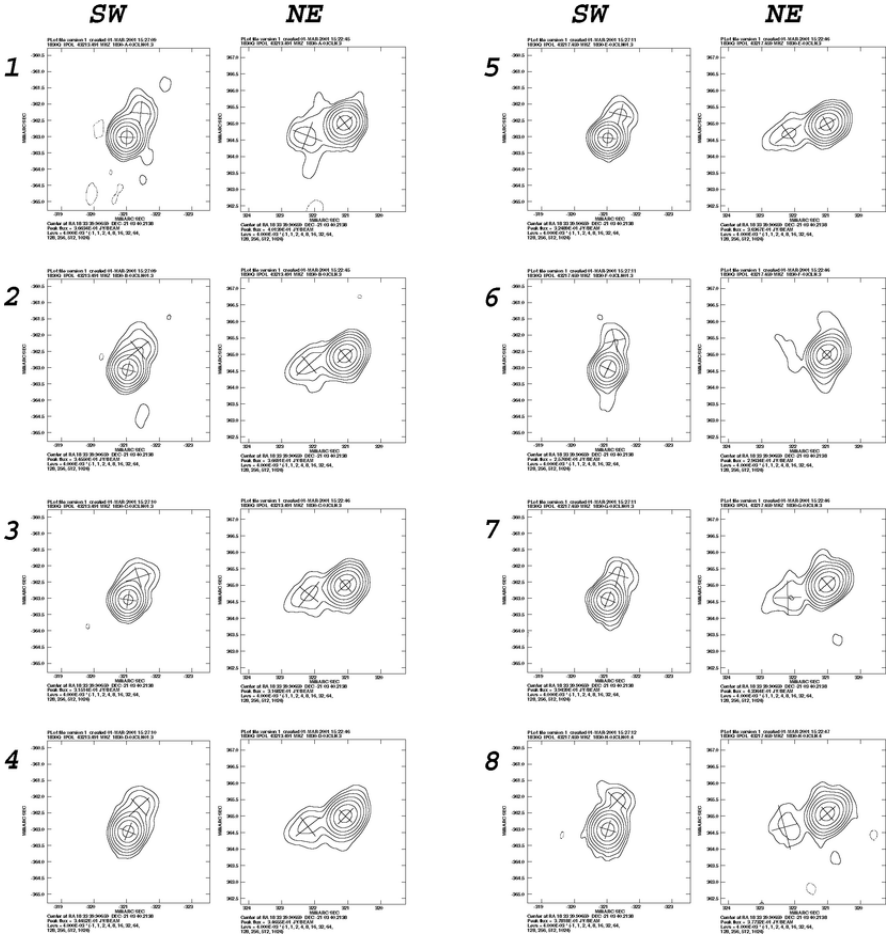

Figure 3.3: The 8-epoch 43 GHz monitoring of PKS 1830-211 performed by Jin *et al.* (2003).

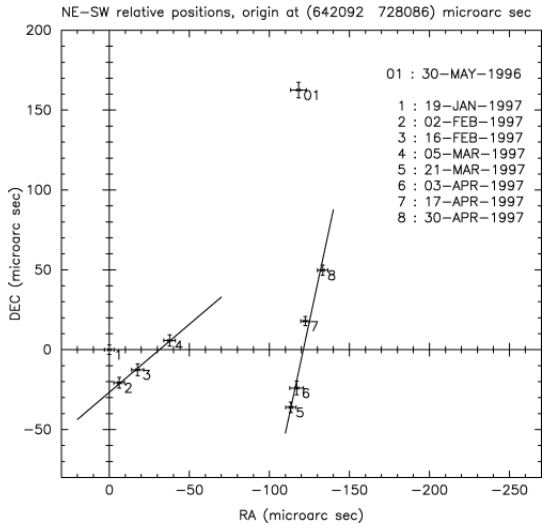

Figure 3.4: Variations in the distance between the two images based on the 8-epoch observations at 43 GHz.

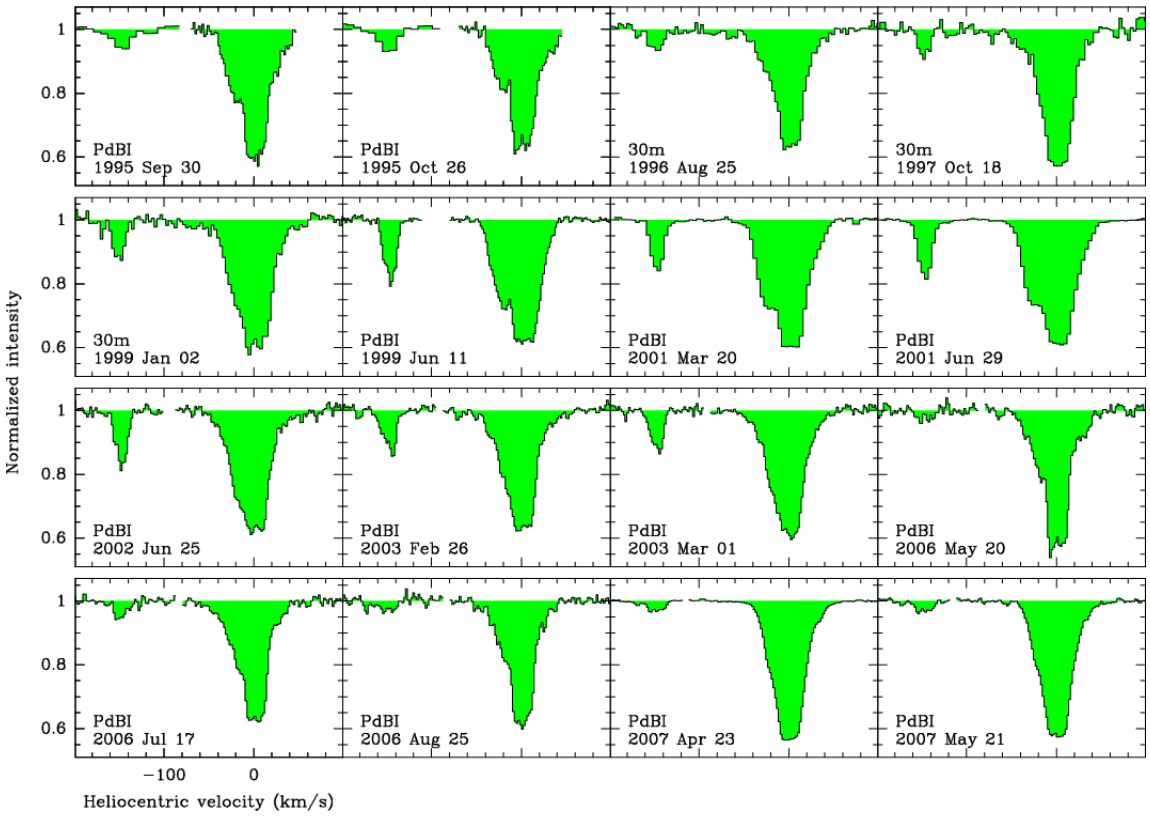

Figure 3.5: A 12-year monitoring of HCO^+ 2-1 absorption line towards PKS 1830-211 using the IRAM 30 m telescope (Muller and Guélin, 2008).

3.1.1 Absorption line measurements

An independent line of evidence for the origin of the observed variation between the two images comes from a decade-long, spectroscopic absorption line monitoring of the two lensed images. Muller and Guélin (2008) performed a 12-year monitoring of HCO^+ 2-1 absorption line towards both the images using the IRAM 30 m telescope and Plateau de Bure Interferometer (PdBI), and found drastic changes in the absorption depth during the entire observation period. The absorption spectra obtained as part of that monitoring program is shown in figure 3.5. In each spectrum, the large absorption trough at $v \sim 0$ km/s corresponds to the HCO^+ 2-1 absorption in the SW image and the faint absorption feature $v \sim -147$ km/s corresponds to the NE image. It can be noticed that the feature corresponding to the NE image is not visible throughout the monitoring period and Muller and Guélin (2008) also notice that changes in the NE feature at different epochs are correlated to the wings in the SW absorption feature leading to the argument that the variation must originate in the background quasar. They also noticed that the observed linewidth of the feature at $v \sim 0$ km/s defied any interpretation given that the lens galaxy is seen nearly face-on.

3.2 PKS 1830-211 as a cosmological probe

3.2.1 T_{CMB} from absorption line measurements

Apart from being useful in determining H_0, PKS 1830-211 has also been used in several other cosmological studies like determining the temperature of the cosmic microwave background (CMB) at redshift z = 0.89. A recent, detailed review of the potential uses of the two lines of sight in PKS 1830-211 can be found in Muller (2011).

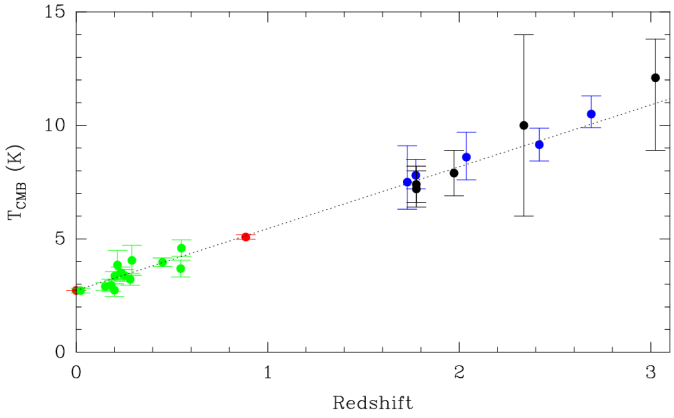

Figure 3.6: Temperature of the cosmic microwave background measured using different probes shown as a function of cosmological redshift. The data point shown in red was obtained using PKS 1830-211 by Muller *et al.* (2013)

Temperature evolution of the cosmic microwave background as a function of redshift is a very important tool to differentiate between different dark energy models. Within the framework of the concordance cosmological model, the present temperature of CMB (T_0) can be related to its temperature at some redshift z as

$$T(z) = T_0(1+z)^{(1-\alpha)} \tag{3.1}$$

where $\alpha = 0$ for the flat concordance cosmological model. By measuring the rotation temperature of many molecular species towards both the lines of sight in PKS 1830-211, Muller *et al.* (2013) estimate a value of T_{CMB}(z=0.89) = 5.08 ± 0.10 K. Figure 3.2.1 shows the measured temperature of CMB at different redshifts and the data point indicated in red corresponds to value determined in the study being discussed here. The dotted line is the best fit curve for the temperature evolution of T_{CMB} and is consistent with the value expected for a flat concordance cosmological model. The effectiveness of this method for determining the temperature of the background radiation can be realized from figure 3.2.1 by comparing the size of the error bars for this measurement with the values determined by other cosmological probes like the Sunyaev-Zeldovich effect (green data points) and absorption line studies towards other quasars (black and blue data points).

3.2.2 Variation of fundamental constants

The lines of sight towards PKS 1830-211 have also been used to study variations in the fundamental constants at high redshifts, namely variations in the proton-to-electron mass ratio (μ). Using a number of inversion lines of ammonia (NH_3), an upper limit to the variation in the proton-to-electron ratio of $(\Delta\mu/\mu) \sim 10^{-6}$ has been estimated (Muller *et al.*, 2011; Henkel *et al.*, 2009). Given that a number of molecular species along with some of their isotopes have been detected towards the SW image, it has been possible to compare the isotopic ratios at z = 0.89 with the values found in the local universe (Muller *et al.*, 2011, 2006). Though these measurements could be biased due to several environmental reasons, the existence of several observable molecular species at a relatively high redshift could have numerous implications in studies concerning astrochemistry.

3.3 Need for a detailed model of PKS 1830-211

It is clear from the arguments cited above (especially §3.1) that the background source cannot be modelled as a simple, stationary continuum source. If the observed variations

are due to a complex source structure as argued, then this would mean that different parts of the spiral arms of the lens are being illuminated by the constantly changing background continuum source. In order to use the lines of sight in PKS 1830-211 as a cosmological probe as discussed in §3.2, it is very important to understand the exact physical extent of the region being illuminated by the background source along both the lines of sight in PKS 1830-211 (i.e.) address model uncertainties on both the image/lens plane and the source plane.

In an attempt towards acheiving a unified model for both the lens galaxy and the source quasar, using new observational constraints, we have refined the existing lens model and have estimated a new value for H_0 using the new model for the lens. Before proceeding to build a new lens model, a brief review of the recent attempts aimed at modelling the lens is presented in §4.1. The new lens model is described in §4.2 and in the later part of the same section, some possible sources of systematics are addressed.

Chapter 4

Modelling PKS 1830-211

4.1 Recent lens models of PKS 1830-211

Though a number of authors have attempted to model the lens towards PKS 1830-211, no model has been able to successfully reproduce the Hubble constant that is consistent with the value derived using other cosmological probes. Large uncertainties in the time delay measured between the two images and in the exact location of the lens galaxy are attributed as the reason for this discrepancy. Though the uncertainty in the time delay could in principle be reduced through long-term monitoring, tackling the problem of the lens position is not straight-forward. Since the line of sight towards PKS 1830-211 traverses through the Galactic plane, deep optical imaging does not produce a clear picture of the lens galaxy and hence it is difficult to identify the exact barycenter of the lens. Thus, no two existing models agree on the location of the lens galaxy and the lens position adopted by various authors is displayed in figure 3.1. In this section, two latest works that model PKS 1830-211 using lens positions obtained from the same HST images are reviewed.

4.1.1 Winn *et al.* (2002)

Although Lehar *et al.* (2000) had detected the lens galaxy using HST observations, they were unable to determine the position of the lens itself. Winn *et al.* (2002) obtained V-band and I-band HST images of PKS 1830-211 and identified different objects in the field of view. Both the images are shown in figure 4.1. The bulge of the galaxy was detected in both the images and was used to determine the position of the lens galaxy. Using the derived lens position, and data from previous observations, the lens was modelled as a Singular Isothermal Ellipsoid (SIE). They obtained the best fit for the observed data using the method described in appendix C and derived a value of 44±8 km/s/Mpc for the Hubble constant assuming Ω_m = 0.3 and Ω_Λ = 0.7 which is a relatively low value for H_0 compared with the value derived using other cosmological probes. Apart from modelling the lens using the new lens position, they also place the lens galaxy on the Tully-Fisher (TF) relation and find that the mass of the lens as determined from the lens modelling to be compatible with the local TF relation as determined by Sakai *et al.* (2000). Though their lens modelling is quite simple, they offer possible sources of error that could misrepresent the lens model. The primary source of concern is the unaccounted mass distribution in the vicinity of the primary lens. Lehar *et al.* (2000) identified four galaxies within 20" from the primary lens and had suggested that a systematic study of these galaxies is required to obtain a good lens model. Assuming a redshift of z ≈ 0.89 for all the four galaxies, Lehar *et al.* (2000) showed that they could have significant influence on the mass model. However, using HST photometry of the nearest lens galaxy (marked G2), Winn *et al.* (2002) argue that this galaxy is located at a shallower redshift than the primary lens and hence has a smaller effect on the lens modelling, but still

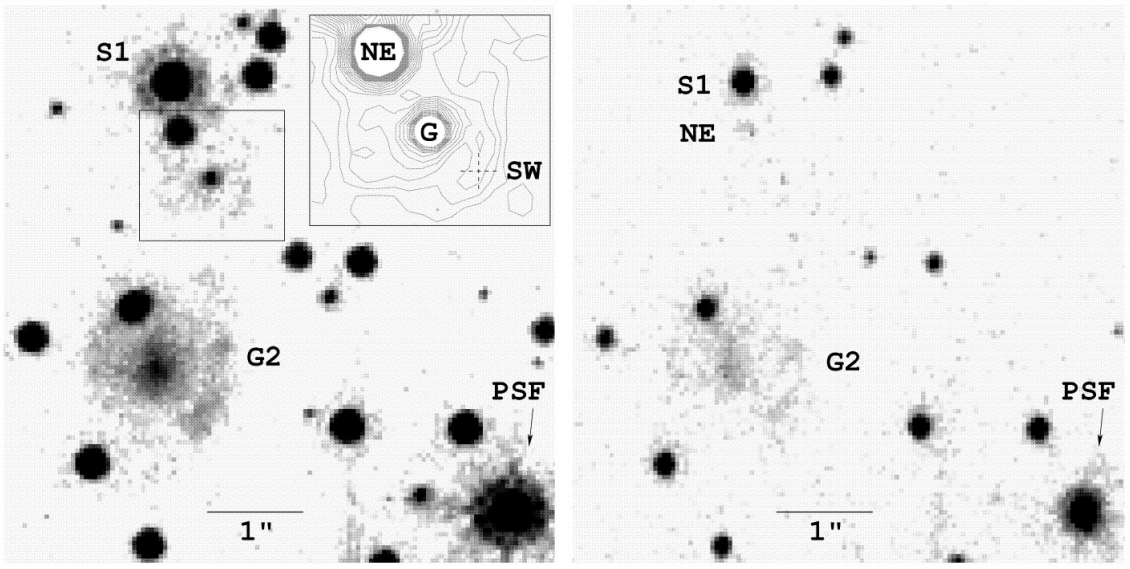

Figure 4.1: I-band (left) and V-band (right) images of PKS 1830-211 obtained by Winn *et al.* (2002) using HST/WFPC2. Both the north-east and the south-west images are marked as NE and SW respectively, and G indicates the lens galaxy.

emphasize that a spectroscopic study of these neighbouring galaxies need to be carried out. Additionally, they also suggest that the lens needs to be modelled in a more realistic fashion by taking into account the contributions from the bulge, the disk and the halo individually.

4.1.2 Courbin *et al.* (2002)

Independent of Winn *et al.* (2002), Courbin *et al.* (2002) identified different object along the line of sight towards PKS 1830-211 using the same HST data as Winn *et al.* (2002) and new observations using Gemini-North. By deconvolving the HST images using the MCS deconvolution algorithm (Courbin *et al.*, 1998), they identified two lens galaxies which are marked G and SP in figure 4.2 with SP being the near-face-on spiral at z=0.89. With these new information about the lens position, they first modelled the lens as a single Pseudo Isothermal Ellipsoid Mass Distribution (PIEMD) Kneib (1993) centered at different positions: G, SP and SA. The model provides a best fit only for the lens centered at G with time delay of 40 days and the lens centered at SA with a 31-day time delay. Next, they proceeded to model the lens with two galaxies centered at positions G and SP assuming both the galaxies to be at z=0.89. They obtained a good fit with a predicted time delay larger than 40 days for $\epsilon \sim 0.2$ and PA $= -50°$ with G being 3.5 times more massive than SP. Upon moving one of the galaxies to a redshift of z = 0.19, a good fit was obtained only for time delays less than 10 days. Given such an uncertain modelling, they concluded that "PKS 1830-211 will remain of little interest in terms of modeling and for the determination of H_0" in the absence of more observational constraints.

Though Winn *et al.* and Courbin *et al.* used the same data set, their independent analysis resulted in significant deviation in their final results which reiterates the fact that a more detailed observational programs supplemented with detailed modelling is required to build a better lens model of PKS 1830-211.

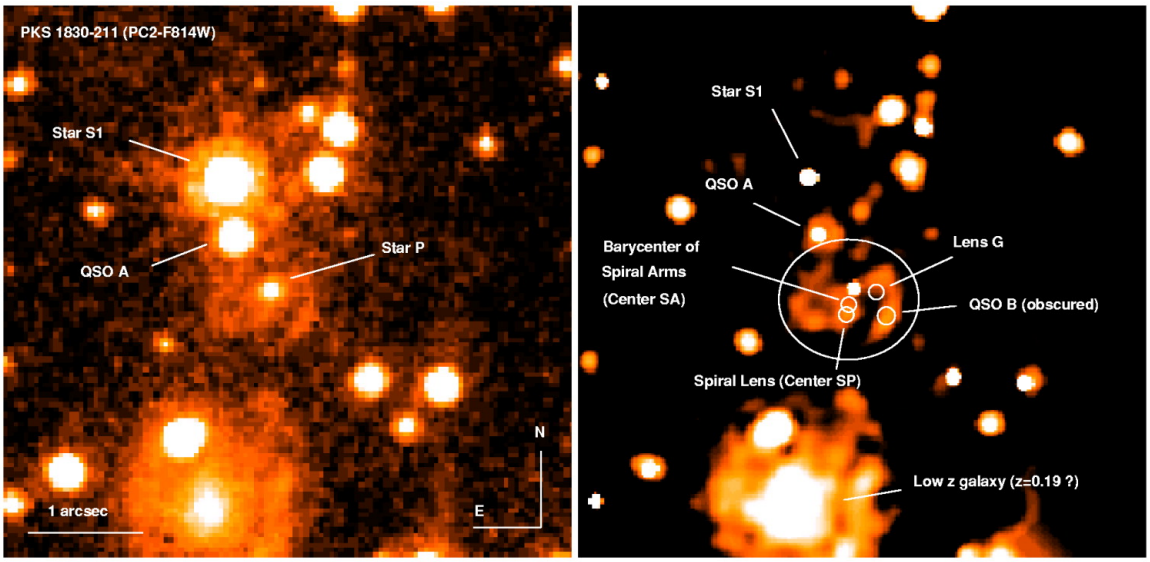

Figure 4.2: *Left:* HST/WFPC2 image of PKS 1830-211 observed with the F814W filter for 6400 s. *Right:* Deconvolved HST image using the MCS deconvolution algorithm. Image: Courbin *et al.* (2002).

4.2 Refined lens model

As explained in chapter 2, a number of mass distributions have been used to model spiral galaxies. In order to find the best model that fits the spiral lens in PKS 1830-211, we model the lens system by considering a variety of lens configurations and single out the one that suits the observations best by minimising the χ^2. Assuming that the source and the produced images are mathematical points, and using both the old and the new observational data published in the literature (table 4.1), we identify the best lens model by using the method of Least Square for each mass distribution. Using the refined lens model, we estimate the value of Hubble constant H_0 and study how the dynamical variations in the background quasar observed by Jin *et al.* (2003) influence the continuum covering fraction by the molecular clouds in the lens galaxy.

Since Winn *et al.* (2002) and Courbin *et al.* (2002) do not agree on a final lens position or lens configuration, we begin by considering all the lens positions discussed in those two papers. For the sake of comparison and better understanding, we use two sets of observations - 'old' and 'new' - to constrain the lens model. The 'old' data set corresponds to the image positions, time delay and the flux ratio measured between the two images that were obtained prior to 2002; the 'new' data set contains values for these parameters that have been observed since the publication of the above two papers. A list of all observational constraints and cosmological values required to compute the lens model is listed in table 4.1. Using these constraints, we perform model fitting for the lens parameters using the method described in appendix C[1].

One of the primary issues, apart from the uncertain lens position, that has largely affected the effectiveness of previous models is the lack of sufficient number of data points required to constrain the lens model. Hence to increase the number of data points as much as possible, we include the value of Hubble constant determined from other cosmological probes as a constraint. But it should be kept in mind that this is not the most optimistic approach to lens modelling since gravitational lens provides an independent verification for the value

[1]A similar, independent χ^2 fit was performed using the *glafic* lens modelling software (Oguri, 2010) and this independent check confirms the result obtained using *lensmodel*.

Table 4.1: Observational constraints for the lens model. All positions are measured with respect to the NE image.

Constraints	**Value**	**Reference**
NE Image	(0,0)	
SW Image (Old)	(0".642, -0".728)±0.001	Jin *et al.* (1999)
Lens position W	(0".328, -0".486)±0.004	Winn *et al.* (2002)
Lens position G	(0".519, -0".511)±0.080	Courbin *et al.* (2002)
Lens position SP	(0".285, -0".722)±0.040	Courbin *et al.* (2002)
Lens position SA	(0".300, -0".610)±0.050	Courbin *et al.* (2002)
Old flux ratio (NE/SW)	1.52±0.05	Lovell *et al.* (1998)
New flux ratio (NE/SW)	1.35±0.14	Muller et al (Private communication)
Old time delay (SW - NE)	26±4 days	Lovell *et al.* (1998)
New time delay (SW - NE)	27.1±0.6 days	Barnacka *et al.* (2011)
Hubble constant	70.2±2.2 km/s/Mpc	Hinshaw *et al.* (2012)

of Hubble constant. In principle, gravitational lens systems can be used independently to constrain H_0, but we choose to use the value of H_0 determined by other cosmological means as an additional data point to constrain the lens model.

4.2.1 Results from model fitting

The results from performing model fitting for each of the lens position listed in table 4.1 are shown in appendix D in tables D.2 – D.5. Each of these tables correspond to model fitting with the SIE lens at four different positions considered above. The first two columns in these tables are the results due to the 'old' data set while the results for the 'new' data set is in the last two columns of these tables. Note that the model fitting procedure gives only the best-fit values and the uncertainties on each of the model fitting parameters were obtained by performing a Monte Carlo analysis.

The outcome of the model fitting procedure can be described in the following manner:

- In the case of position 'W', when H_0 is not used as a constraint, the χ^2 fit is exact but predicts $H_) = 44.25$ km/s/Mpc. When H_0 is used as a constraint, the best fit model gives a time delay of 16.25 which is significantly lower than the observed value. In the case of new observational constraints, the time delay improves slightly but is still inconsistent with the observed value.

- The results for both the lens positions 'G' and 'SP' are similar to that of 'W' except for the fact that they predict a time delay which is significantly larger than the observed value.

- In general, the lens positions 'W', 'G' and 'SP' produce $\chi^2 \geq 70$.

- In the case of lens position 'SA', we find $\chi^2 = 0.306$ for 1 degree of freedom which corresponds to 58% probability to exceed.

- Of the four lens models, the model with lens at positiion 'SA' appears to fit the 'new' data set best though giving a relatively high value for the lens ellipticity. In previous analysis (for example Winn *et al.* (2002)), it has been argued that since the lens galaxy is a near-face-on spiral galaxy, the lens galaxy must have a very low ellipticity. However, it is not clear if the orientation of the spiral disk can be used as a proxy for the ellipticity of the lens given the uncertain shape of the dark matter halo around the galaxy. Results from cosmological simulations also indicate that at higher redshifts,

Table 4.2: New lens model

Parameter	**Value**	Reference
NE Image	(0,0)	
SW Image	(0.642,0.728)±0.003	Jin *et al.* (1999)
Lens position	(0".300, -0".610)±0.050	Position SA in Courbin *et al.* (2002)
Flux ratio	1.35±0.14	Muller et al (Private communication)
Time delay (t_{NE} - t_{SW})	27.1±0.6 days	Barnacka *et al.* (2011)
H_0	76 ± 28 km/s/Mpc	
Einstein angle b (arcsec)	0.513 ± 0.028	
Lens ellipticity e	0.29 ± 0.09	
Lens position angle	$97° \pm 18°$	
Source position	$(0.210, -0.504) \pm 0.045$	

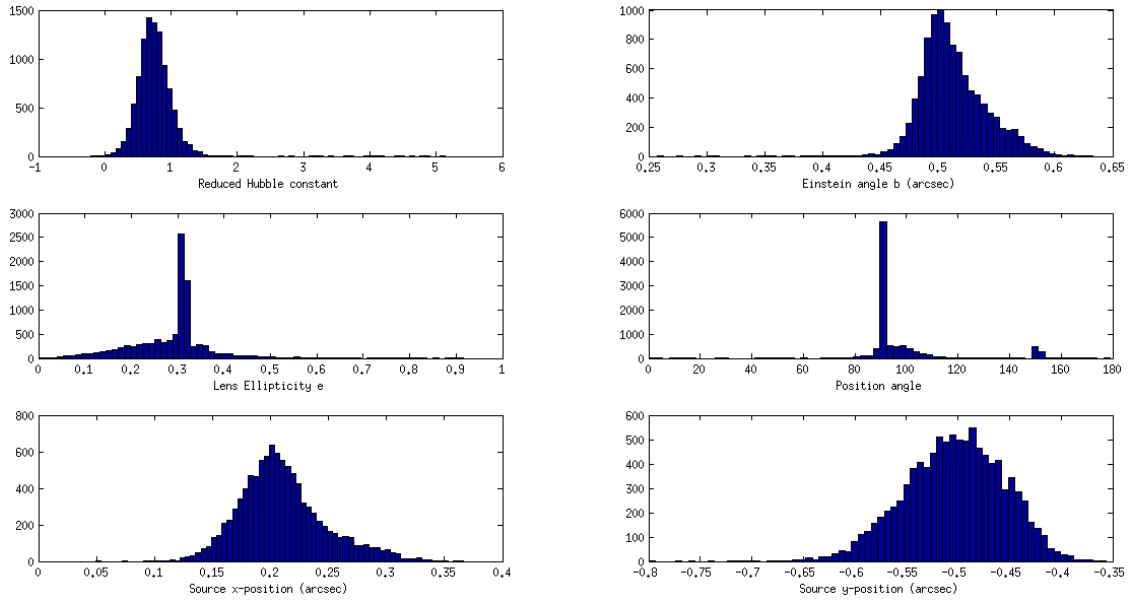

Figure 4.3: Uncertainties on each model parameter derived using a Monte Carlo analysis.

the angular momentum vectors of the disk and the dark matter halo are misaligned (van den Bosch *et al.*, 2002).

When *lensmodel* is used to perform χ^2 fitting, it returns only the best fit values and not the error bars associated with each of the model parameters. In order to estimate the error bars on each of these best-fit model parameters, we first create a list of randomly drawn source-lens configurations using a Gaussian Random Number Generator such that each of the drawn value is restricted to be within the range dictated by observations. For each of the randomly drawn configuration, we then compute the corresponding values of model parameters. The final best fit values for the lens model at position 'SA' along with their uncertainties are presented in table 4.2.1.

Figure 4.4 shows the comparison between the value of H_0 derived using our model of PKS 1830-211 with the value estimated using other gravitational lenses. The values of H_0 determined using other gravitational lenses are also presented in table F.1.

4.2.2 Microlensing due to stars

A robust model of a galaxy-scale lens must account for possible microlensing effects by individual stars in the lens galaxy. Their influence is primarily felt in the flux ratios observed

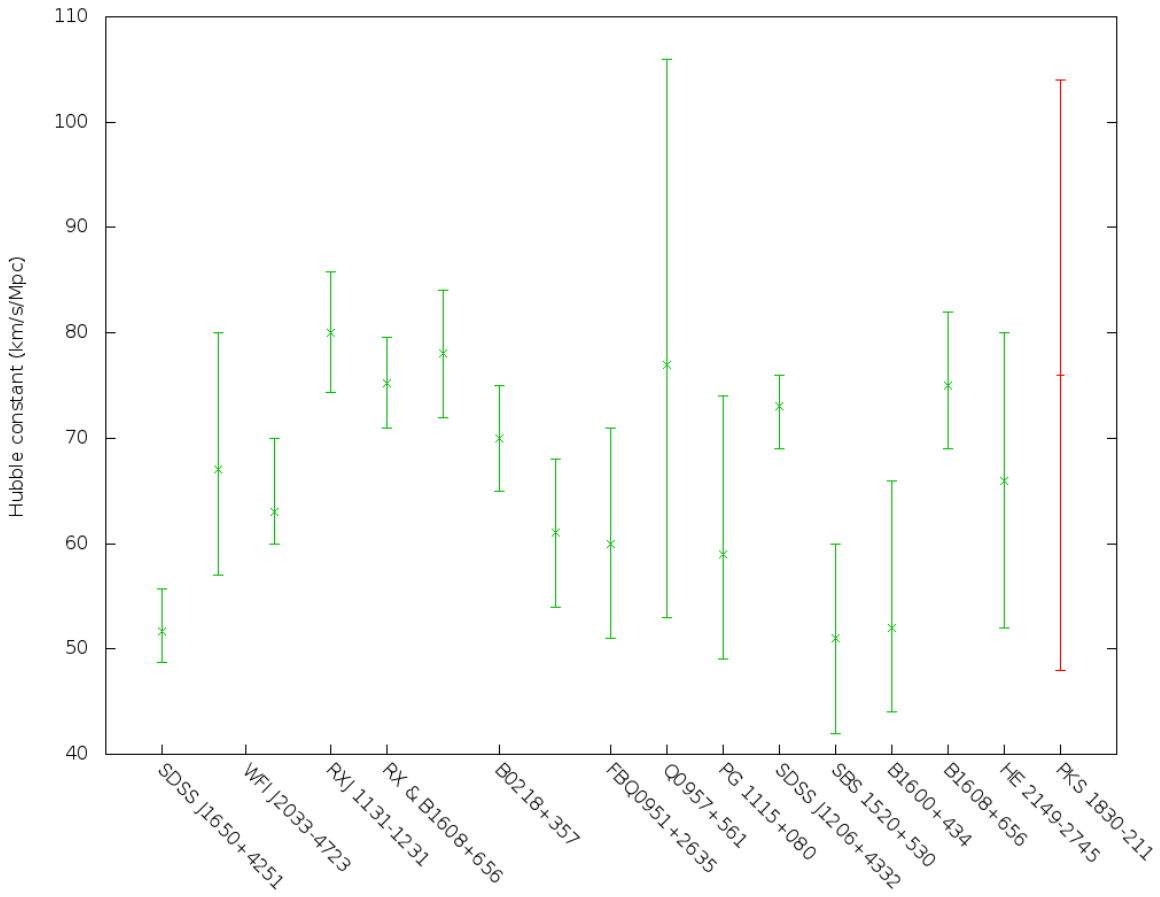

Figure 4.4: Comparison of H_0 estimated using the refined lens model for PKS 1830-211 (shown in red) with the value estimated using other gravitational lenses (shown in green).

between the images and possible distortions in the shapes of the critical and the caustic lines. In principle, it is possible to check whether a given point-like lens affects the lens modelling, without elaborate calculations, by simply comparing the angular size of the lens and the projected Einstein radius of the point source. If the background source is larger than the Einstein radius of each star, then microlensing effects on the images will be negligible and can be ignored in the modelling.

In our case, if the mass of each star is assumed to be within the range $1 \leq M_{star}/M_{\odot} \geq 30$ and if stars are modelled as a point mass lens, the Einstein radius of an individual star is

$$R_E = \begin{cases} 1.58 \text{ uas} & M_{star}/M_{\odot} = 1 \\ 4.2 \text{ uas} & M_{star}/M_{\odot} = 30 \end{cases} \tag{4.1}$$

These angles, on the image plane, correspond to 0.013 pc and 0.067 pc respectively. Thus, the Einstein angle of individual stars in the lens galaxy are much smaller than the AGN and hence microlensing effects can be neglected.

4.2.3 Lensing due to nearby galaxies

In order to have a robust lens model of any gravitational lens, it is important to estimate the influence of external mass present near the main lens galaxy. In figure 4.2, a spiral galaxy can be seen quite close to the two lines of sight towards PKS 1830-211. Apart from this lens, Lehar *et al.* (2000) identified 6 galaxies within a field of view of 20" from the main lens

galaxy (see table 2 of Lehar *et al.* (2000)). Thus, it is important to estimate the magnitude of influence exerted by these galaxies at the position of the NE and the SW images. This can be done by computing the convergence κ at the image positions due to some secondary lens. If $\kappa \geq 1$, the lens under consideration would certainly have a strong influence on the images and hence must be incorporated into the primary lens modelling; if not, the secondary galaxy contributes to the weak lensing and can either be included or neglected depending on the context under which the primary lens modelling is performed.

In the case of the secondary lens visible in figure 4.2, no dedicated observation have been performed for this galaxy and hence both the exact redshift and a good mass estimate is not available. Winn *et al.* (2002) Thus κ is determined for both the NE and the SW images for a wide range of values for the mass and the redshift of the galaxy under consideration. Since this secondary lens is relatively far away from the image positions than the main lens galaxy, the exact mass model used to define this galaxy will not affect the outcome of this exercise significantly. Therefore, for the sake of simplicity, the secondary spiral lens is modelled as a singular isothermal sphere (SIS).

For an SIS lens, convergence κ is given as (see section 2.2.1),

$$\kappa(\boldsymbol{\theta}) = 2\pi\left(\frac{\sigma_v}{c}\right)^2 \frac{D_{ds}}{D_s}\frac{1}{\boldsymbol{\theta}} \tag{4.2}$$

where σ_v is the 1-d velocity dispersion of the SIS model, c is the velocity of light, D_{ds} and D_s are the source-to-lens observer-to-lens distances respectively, and $\boldsymbol{\theta}$ is the two dimensional vector on the image plane. If $\boldsymbol{\theta_I}$ and $\boldsymbol{\theta_L}$ represent the image and the lens position, then the above equation becomes

$$\kappa(|\boldsymbol{\theta_I} - \boldsymbol{\theta_L}|) = 2\pi\left(\frac{\sigma_v}{c}\right)^2 \frac{D_{ds}}{D_s}\frac{1}{|\boldsymbol{\theta_I} - \boldsymbol{\theta_L}|}. \tag{4.3}$$

Since κ is a dimensionless quantity, the angular distance between the lens and the image $|\boldsymbol{\theta_I} - \boldsymbol{\theta_L}|$ must be in radians.

The spiral galaxy under question is located at (-0".24,-2".48)±0".02 with respect to the NE image. Using this secondary lens position, convergence is computed at the two image positions using the equation (4.3) by varying the lens redshift between 0.001 and 2.5, and velocity dispersion between 100 km/s and 300 km/s. The computed values for κ is displayed in fig. 4.2.3 as a function of the lens redshift and the SIS velocity dispersion. Note that κ is much smaller than 1 at both NE and SW image positions which leads us to conclude that this galaxy does not have any strong influence on the primary lens. It can also be noticed that the SW image has a slightly higher value of κ for each (z_{lens},σ_v) pair. This is due to the fact that the secondary lens is situated closer to the SW image than the NE image. It can also be seen from the maps in fig. 4.2.3 that for a fixed velocity dispersion, κ at a given image position decreases with increasing lens redshift. This is due to the fact that κ is directly proportional to the distance between the lens and the source which in turn decreases with increasing lens redshift.

Since the closest galaxy in the field of view has negligible effect on the main lens towards PKS 1830-211, it can be inferred that the other lens candidates identified within 20" from the main lens by Lehar *et al.* (2000) have even smaller impact than the one considered above. However, it should be kept in mind that if the secondary galaxy considered above is relatively massive ($\sigma_v \geq 300$) km/s and at shallower redshifts ($z \approx 0.1$), the weak lensing effects start to become stronger and hence must be included in the lens modelling.

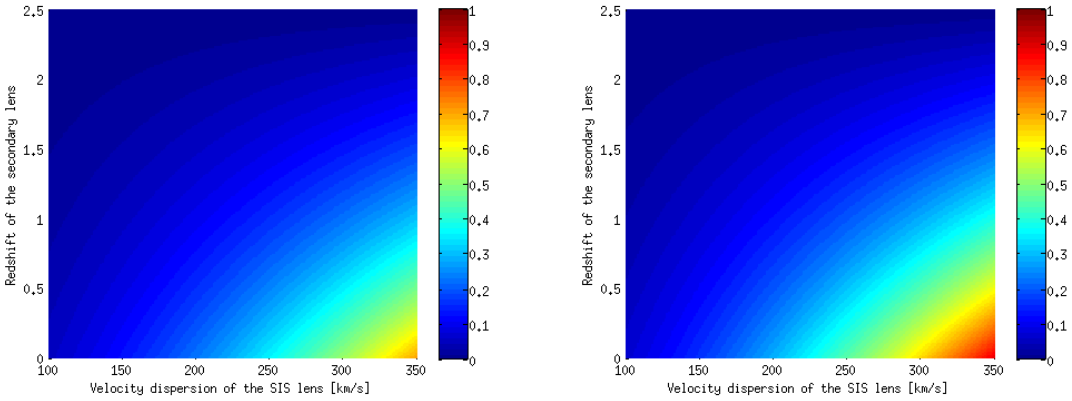

Figure 4.5: Convergence due to the nearby spiral galaxy at the NE (left) and the SW (right) image positions. For a large part of the parameter space, $\kappa \ll 1$ and it approaches 1 only for a very massive ($\sigma_v \geq 300$ km/s) lens at shallower redshifts (z $\sim$ 0.2).

Table 4.3: Results from model fitting using a multicomponent source as shown in epoch 1 of figure 3.3.

Lens position	χ^2	σ **(km/s)**	**e**	**PA**	**|Δ x| (mas)**	**|Δy| (mas)**
W	196.07	190.47	0.0902	88.23	3.7581	5.1048
G	204.89	185.21	0.221	-33.53	8.5548	8.358
SP	513.3	202.71	0.551	103.1	0.2918	0.3217
SA	0.044	194.8	0.344	99.74	0.3305	0.0004

4.3 Model fitting with a multicomponent source

As discussed in §3.1, it is clear from VLBI observations that the background source in PKS 1830-211 can be resolved in to multiple milli-arc-sec components. Recently Suyu (2012) showed that if the positions of multiple components in both the images of a two-image lens can be determined with mas precision, they offer a much better constraint on the lens model than considering a single component source. Though the background quasar has been resolved into multiple components, the positions of each of these components must be known with mas precision and hence cannot be used to improve the lens model any further in the case of PKS 1830-211. However, they can be still be used to check the consistency of the results of the previous model fitting and, for a given lens model, can be used to find the unlensed position of each source component. In this section, we repeat the model fitting – for each lens position – with the additional positional information concerning the "knot" seen in both NE and SW images with respect to the "core" in the respective images at 43 GHz (see figure 3.3)[2]. The results from this analysis is shown in figure 4.3.

Once again, it can be seen that the lens at position SA fares better than all other lens positions. Though the analysis performed here does not improve the lens model, future observations (see section §5.1) will be able to resolve the background source with mas precision and hence will be able to provide additional constraints to improve the lens model.

[2]Since the angular separation between the core and the knot is very small, *lensmodel* could not be used to perform model fitting. Instead, the software package *glafic* is used.

Chapter 5

Future Prospects

In this chapter, we discuss some of the key ideas that can be used in the near future to improve the lens and the source model of PKS 1830-211. There are two principle ways in which the lens model can be improved: (i) increasing the number of available observational constraints and (ii) using extended source features in the analysis. A brief discussion on using either of these ways for improving the lens model for PKS 1830-211 is presented in sections §5.1 and §5.2.

5.1 Additional observational constraints

From the content presented in chapter 3, though a smooth mass distribution like SIE appears to describe the macro-lens model well, a detailed lens model of a spiral galaxy requires representing each component of the lens using an individual mass distribution. Such a model should also account for the existence of dark matter sub-structure in the lens galaxy as well. Modelling a lens with such a complex internal structure increases the number of free parameters significantly and hence cannot be attempted with the current observations available (excluding the extended features) for PKS 1830-211. Recently Fadely *et al.* (2010) improved the lens model of the two-image lens Q0957+561 significatly by identifying 26 new lensed source components. In order to perform a similar analysis for PKS 1830-211, detailed high resolution observations are required to determine the positions of subcomponents in each lensed images with mas precision. Though we were able to attempt such a modelling using multiple components detected in Jin *et al.* (2003), we were unable to extract any scientific information from it. Given recent developments in high resolution radio telescopes and interferometers, it might be possible to detect more subcomponents in both the images of PKS 1830-211 with very high astrometric precision which can lead to a better constrained lens model. However, as Jin *et al.* (2003) detected time dependent variations in the background quasar, a long term monitoring of both the images is required to extract a detailed picture of the source plane.

In order to procure high resolution observations that would facilitate improved modelling of both the lens and the source structures, we have proposed a two-epoch dual-frequency VLBA observations of both the NE and SW images at 94.6 GHz and 23.65 GHz. Since the associated jet of the bright core has a steep spectral index, observations at two different frequencies will enable us to the differentiate between the continuum emission contributed by both the core and the jet. At 94.6 GHz, the synthesized beam is 0.60×0.15 mas which has a physical extend of roughly a parsec at $z = 0.89$ thus making these observations the highest resolution observations ever performed for PKS 1830-211.

Apart from detecting multiple subcomponents in both the images, the twin-epoch VLBA observations offer very good resolution in both spatial and velocity dimensions and hence will enable us not only to study the background quasar but also to probe the molecular clouds

in the lens galaxy that cover the background continuum source thereby putting a tight constraint on the systematics that could in principle affect previous cosmological measurements like the temperature of the cosmic microwave background.

5.2 Extended images

Though four-image lenses provide more data points/positional constraints than two-image lenses, four-image lenses cannot constrain the the slope of the radial profile of the lens mass distribution since all images form at roughly the same radii from the lens center. In the case of two-image lenses, since both the images generally form at different galactocentric radii, they provide additional information about the radial mass profile of the lens galaxy. However as both the images of a two-image lens and the center of the lens galaxy itself are roughly aligned along a straight line, these lenses cannot be used to study the angular profile of the lens mass distribution.

If the two-image lens has extended ring-like feature along with bright cores, the combination of the two can be used in unison to provide detailed information about both the radial and the angular profile of the lens mass distribution. Since all the lens models – including the one that is discussed in this thesis – have considered only the point-like images, employing the pseudo-Einstein ring observed at 5 GHz in the lens model could turn out to be quite interesting. In the model fitting procedure performed in the previous chapter, we had placed our SIE lens at four different lens positions and studied which of those lens positions provide a better fit to the observational data. If we have more observational constraints (like the pseudo Einstein ring) apart from what we have at the moment, the lens position can be allowed to vary within the region bound by the radio ring. Such a procedure would provide a better constraint on the lens position which in turn would reduce the uncertainty on the estimated value of H_0. The importance of including extending features in lens model fitting and the mathematical theory behind using Einstein rings as constraints can be found in Kochanek *et al.* (2001). There are numerous ways in which extended features can be included in the lens modelling and a short description about three such techniques are discussed in this section.

Including extended features in lens modelling can be done using *lensmodel* either by fitting a ring to the entire extended structure or by fitting curves corresponding to different images that are produced by the lens. Smith *et al.* (2005) had used the curve fitting feature of *lensmodel* to model strong lensing by the nearby elliptical lens ESO 325-G004. As a part of this thesis, we tried to improve the lens model of PKS 1830-211 by fitting a closed curve to the 5 GHz radio ring. However, due to technical difficulties with the *lensmodel* package, such an attempt was not fruitful and the exact reason for this failure is yet to be determined.

Soon after the above mentioned failed attempt to improve the lens model, Muller (Private communication) suggested a new approach to model fitting which when implemented increases the total number of available constraints significantly. The principle idea behind this approach is to simulate a vast number of mock observations of a lensed quasar by varying all model parameters and then compare each of the simulated images with the observed 5 GHz map of PKS 1830-211 using a simple χ^2 statistic. Though such a procedure is computationally very expensive, the total number of available constraints is as large as the number of pixels in the images being compared. As a part of this thesis, the above mentioned procedure was implemented and a brief overview of the code is presented in appendix E. Though the algorithm has been implemented, we were unable to perform the required model fitting analysis for PKS 1830-211 due to the unavailability of the reduced 5 GHz Merlin image and hence the application of this code is left for future work.

Recently, Suyu (2012) (also see Suyu *et al.* (2006)) has shown through simulations that Bayesian techniques can be used to solve for both the source intensity distribution and the

lens mass distribution simultaneously for twin-imaged gravitational lenses thereby overcoming the so-called radial profile slope degeneracy. Though such techniques have been used extensively to reconstruct the lens and the source structures based on optical observations (see Suyu *et al.* (2009, 2013) and references therein), as far as we could find, such techniques have not been used for extended radio images. Given that there are more twin-imaged gravitational lenses than four-image lenses (Oguri, 2007) and that future surveys are expected to find more two-image lenses than four-image ones (Oguri and Marshall, 2010), applying such an analysis to the radio Einstein ring of PKS 1830-211 could be very interesting both for the lens and the source models of PKS 1830-211 and for the technique itself.

Chapter 6

Conclusion

Though initially appears as a simple two-image gravitational lens, the lensed quasar PKS 1830-211 appears to have quite a lot of interesting features hidden up its sleave. Though the quasar was identified to be gravitationally lensed in the late 1980s, no lens model has been able to explain all the observed physical phenomena associated with the lens galaxy and the background source. As an initial attempt towards achieving a unified lens model for both the lens galaxy and the source in PKS 1830-211, we have refined the existing lens model based on high resolution observations that have been performed since the year 2002.

The primary outcome of the analysis performed in this thesis are:

- Of the four possible lens positions suggested in previous models (Winn *et al.*, 2002; Courbin *et al.*, 2002), the lens position 'SA' appears to fit the observational data better than the other positions.

- Though the best fit lens model has a large ellipticity ($e = 0.29 \pm 0.09$) for a near-face-on spiral galaxy, it does not contradict the findings as the spiral disks are generally misaligned with the dark matter halo and hence cannot be used as a tracer for the ellipticity of the halo, especially at higher redshifts (for example, see van den Bosch *et al.*, 2002).

- Using the refined lens model, we estimate a value for the Hubble constant to be $H_0 = 76 \pm 28$ km/s/Mpc. The uncertainty on the value of H_0 scales linearly with the uncertainty on the lens position and hence reducing the uncertainty on the latter through future observations could improve the value of H_0 estimated using PKS 1830-211.

- The galaxy suspected to be at redshift $z = 0.19$ appears to exhibit no strong lensing effects at both image positions.

- Though we attempted to incorporate the pseudo-Einstein ring into the lens modelling, our attempt was futile due to technical difficulties with the *gravlens* software.

Finally, we conclude this thesis by strongly insisting that the complexity of the model for both the lens galaxy and the background quasar cannot be improved without either new high resolution observations or incorporating the pseudo-Einstein ring in the lens modelling procedure.

Bibliography

Barkana, R. (1998). Fast Calculation of a Family of Elliptical Mass Gravitational Lens Models. *ApJ*, **502**, 531.

Barnacka, A., Glicenstein, J.-F., and Moudden, Y. (2011). First evidence of a gravitational lensing-induced echo in gamma rays with Fermi LAT. *A&A*, **528**, L3.

Bartelmann, M. (1996). Arcs from a universal dark-matter halo profile. *A&A*, **313**, 697–702.

Bernstein, G. and Fischer, P. (1999). Values of H_0 from Models of the Gravitational Lens 0957+561. *AJ*, **118**, 14–34.

Blake, C., Brough, S., Colless, M., Contreras, C., Couch, W., Croom, S., Croton, D., Davis, T. M., Drinkwater, M. J., Forster, K., Gilbank, D., Gladders, M., Glazebrook, K., Jelliffe, B., Jurek, R. J., Li, I.-h., Madore, B., Martin, D. C., Pimbblet, K., Poole, G. B., Pracy, M., Sharp, R., Wisnioski, E., Woods, D., Wyder, T. K., and Yee, H. K. C. (2012). The WiggleZ Dark Energy Survey: joint measurements of the expansion and growth history at z < 1. *MNRAS*, **425**, 405–414.

Braatz, J., Reid, M., Kuo, C.-Y., Impellizzeri, V., Condon, J., Henkel, C., Lo, K. Y., Greene, J., Gao, F., and Zhao, W. (2013). Measuring the Hubble constant with observations of water-vapor megamasers. In R. de Grijs, editor, *IAU Symposium*, volume 289 of *IAU Symposium*, pages 255–261.

Burud, I., Hjorth, J., Jaunsen, A. O., Andersen, M. I., Korhonen, H., Clasen, J. W., Pelt, J., Pijpers, F. P., Magain, P., and Østensen, R. (2000). An Optical Time Delay Estimate for the Double Gravitational Lens System B1600+434. *ApJ*, **544**, 117–122.

Burud, I., Courbin, F., Magain, P., Lidman, C., Hutsemékers, D., Kneib, J.-P., Hjorth, J., Brewer, J., Pompei, E., Germany, L., Pritchard, J., Jaunsen, A. O., Letawe, G., and Meylan, G. (2002a). An optical time-delay for the lensed BAL quasar HE 2149-2745. *A&A*, **383**, 71–81.

Burud, I., Hjorth, J., Courbin, F., Cohen, J. G., Magain, P., Jaunsen, A. O., Kaas, A. A., Faure, C., and Letawe, G. (2002b). Time delay and lens redshift for the doubly imaged BAL quasar SBS 1520+530. *A&A*, **391**, 481–486.

Cabré, A., Vikram, V., Zhao, G.-B., Jain, B., and Koyama, K. (2012). Astrophysical tests of gravity: a screening map of the nearby universe. *Journal of Cosmology and Astroparticle Physics*, **7**, 34.

Chengalur, J. N., de Bruyn, A. G., and Narasimha, D. (1999). HI and OH absorption at z=0.89. *A&A*, **343**, L79–L82.

Chwolson, O. (1924). Über eine mögliche Form fiktiver Doppelsterne. *Astronomische Nachrichten*, **221**, 329.

Colless, M., Beutler, F., and Blake, C. (2013). Measuring H_0 from the 6dF Galaxy Survey and future low-redshift surveys. In R. de Grijs, editor, *IAU Symposium*, volume 289 of *IAU Symposium*, pages 319–322.

Courbin, F., Lidman, C., Frye, B. L., Magain, P., Broadhurst, T. J., Pahre, M. A., and Djorgovski, S. G. (1998). Image Deconvolution of the Radio Ring PKS 1830-211. *ApJL*, **499**, L119.

Courbin, F., Meylan, G., Kneib, J.-P., and Lidman, C. (2002). Cosmic Alignment toward the Radio Einstein Ring PKS 1830-211? *ApJ*, **575**, 95–102.

Dalal, N. and Kochanek, C. S. (2002). Direct Detection of Cold Dark Matter Substructure. *ApJ*, **572**, 25–33.

Einstein, A. (1936). Lens-Like Action of a Star by the Deviation of Light in the Gravitational Field. *Science*, **84**, 506–507.

Fadely, R., Keeton, C. R., Nakajima, R., and Bernstein, G. M. (2010). Improved Constraints on the Gravitational Lens Q0957+561. II. Strong Lensing. *ApJ*, **711**, 246–267.

Freedman, W. L., Madore, B. F., Gibson, B. K., Ferrarese, L., Kelson, D. D., Sakai, S., Mould, J. R., Kennicutt, Jr., R. C., Ford, H. C., Graham, J. A., Huchra, J. P., Hughes, S. M. G., Illingworth, G. D., Macri, L. M., and Stetson, P. B. (2001). Final Results from the Hubble Space Telescope Key Project to Measure the Hubble Constant. *ApJ*, **553**, 47–72.

Freedman, W. L., Madore, B. F., Scowcroft, V., Burns, C., Monson, A., Persson, S. E., Seibert, M., and Rigby, J. (2012). Carnegie Hubble Program: A Mid-infrared Calibration of the Hubble Constant. *ApJ*, **758**, 24.

Garrett, M. A., Nair, S., Porcas, R. W., and Patnaik, A. R. (1997). Multi-epoch VLBA 15 and 43 GHz observations of the gravitational lens PKS 1830-211: extending VLBI towards the micro-arcsecond scale. *Vistas in Astronomy*, **41**, 281–285.

Garrett, M. A., Leppaenen, K., Porcas, R. W., Patnaik, A. R., Nair, S., and Teraesranta, H. (1998). PKS 1830-211: VLBA lambda 7mm Polarization Observations. In J. A. Zensus, G. B. Taylor, and J. M. Wrobel, editors, *IAU Colloq. 164: Radio Emission from Galactic and Extragalactic Compact Sources*, volume 144 of *Astronomical Society of the Pacific Conference Series*, page 313.

Golse, G. and Kneib, J.-P. (2002). Pseudo elliptical lensing mass model: Application to the NFW mass distribution. *A&A*, **390**, 821–827.

Guirado, J. C., Jones, D. L., Lara, L., Marcaide, J. M., Preston, R. A., Rao, A. P., and Sherwood, W. A. (1999). Dual-frequency VLBI observations of the gravitational lens system PKS 1830-211. *A&A*, **346**, 392–396.

Henkel, C., Menten, K. M., Murphy, M. T., Jethava, N., Flambaum, V. V., Braatz, J. A., Muller, S., Ott, J., and Mao, R. Q. (2009). The density, the cosmic microwave background, and the proton-to-electron mass ratio in a cloud at redshift 0.9. *A&A*, **500**, 725–734.

Hinshaw, G., Larson, D., Komatsu, E., Spergel, D. N., Bennett, C. L., Dunkley, J., Nolta, M. R., Halpern, M., Hill, R. S., Odegard, N., Page, L., Smith, K. M., Weiland, J. L., Gold, B., Jarosik, N., Kogut, A., Limon, M., Meyer, S. S., Tucker, G. S., Wollack, E., and Wright, E. L. (2012). Nine-Year Wilkinson Microwave Anisotropy Probe (WMAP) Observations: Cosmological Parameter Results. *ArXiv e-prints*.

Hogg, D. W. (1999). Distance measures in cosmology. *arXiv:astro-ph/9905116v4*.

Jain, B. and Khoury, J. (2010). Cosmological tests of gravity. *Annals of Physics*, **325**, 1479–1516.

Jakobsson, P., Hjorth, J., Burud, I., Letawe, G., Lidman, C., and Courbin, F. (2005). An optical time delay for the double gravitational lens system FBQ 0951+2635. *A&A*, **431**, 103–109.

Jauncey, D. L., Reynolds, J. E., Tzioumis, A. K., Muxlow, T. W. B., Perley, R. A., Murphy, D. W., Preston, R. A., King, E. A., Patnaik, A. R., Jones, D. L., Meier, D. L., Bird, D. J., Blair, D. G., Bunton, J. D., Clay, R. W., Costa, M. E., Duncan, R. A., Ferris, R. H., Gough, R. G., Hamilton, P. A., Hoard, D. W., Kemball, A., Kesteven, M. J., Lobdell, E. T., Luiten, A. N., Mcculloch, P. M., Murray, J. D., Nicholson, G. D., Rao, A. P., Savage, A., Sinclair, M. W., Skjerve, L., Taaffe, L., Wark, R. M., and White, G. L. (1991). An unusually strong Einstein ring in the radio source PKS1830 - 211. *Nature*, **352**, 132–134.

Jin, C., Garrett, M. A., Nair, S., Porcas, R. W., and Patnaik, A. R. (1999). Changes in the angular separation of the lensed images PKS 1830-211 NE & SW. *Nature*, **43**, 767–771.

Jin, C., Garrett, M. A., Nair, S., Porcas, R. W., Patnaik, A. R., and Nan, R. (2003). Changes in the measured image separation of the gravitational lens system PKS 1830-211. *MNRAS*, **340**, 1309–1316.

Jones, D. L., Preston, R. A., Murphy, D. W., Jauncey, D. L., Reynolds, J. E., Tzioumis, A. K., King, E. A., McCulloch, P. M., Lovell, J. E. J., Costa, M. E., and van Ommen, T. D. (1996). Interstellar Broadening of Images in the Gravitational Lens PKS 1830-211. *ApJL*, **470**, L23.

Kayser, R. and Schramm, T. (1988). Imaging procedures for gravitational lenses. *A&A*, **191**, 39–43.

Kazin, E. A., Sanchez, A. G., Cuesta, A. J., Beutler, F., Chuang, C.-H., Eisenstein, D. J., Manera, M., Padmanabhan, N., Percival, W. J., Prada, F., Ross, A. J., Seo, H.-J., Tinker, J., Tojeiro, R., Xu, X., Brinkmann, J., Joel, B., Nichol, R. C., Schlegel, D. J., Schneider, D. P., and Thomas, D. (2013). The Clustering of Galaxies in the SDSS-III Baryon Oscillation Spectroscopic Survey: Measuring H(z) and D_A(z) at z = 0.57 with Clustering Wedges. *ArXiv e-prints*.

Keeton, C. (2001). Computational Methods for Gravitational Lensing. *eprint arXiv:astro-ph/0102340*.

Keeton, C. R. and Kochanek, C. S. (1998). Gravitational Lensing by Spiral Galaxies. *ApJ*, **495**, 157.

Kneib, J.-P. (1993). *Ph.D. Thesis, Universite Paul Sabatier, Toulouse*.

Kochanek, C. S. and Narayan, R. (1992). LensClean - an algorithm for inverting extended, gravitationally lensed images with application to the radio ring lens PKS 1830-211. *ApJ*, **401**, 461–473.

Kochanek, C. S., Keeton, C. R., and McLeod, B. A. (2001). The Importance of Einstein Rings. *ApJ*, **547**, 50–59.

Koopmans, L. V. E. and de Bruyn, A. G. (2005). HI kinematics in a massive spiral galaxy at z= 0.89. *MNRAS*, **360**, L6–L9.

Koopmans, L. V. E., de Bruyn, A. G., and Jackson, N. (1998). The edge-on spiral gravitational lens B1600+434. *MNRAS*, **295**, 534.

Koopmans, L. V. E., Treu, T., Fassnacht, C. D., Blandford, R. D., and Surpi, G. (2003). The Hubble Constant from the Gravitational Lens B1608+656. *ApJ*, **599**, 70–85.

Kormann, R., Schneider, P., and Bartelmann, M. (1994). Isothermal elliptical gravitational lens models. *A&A*, **284**, 285–299.

Lee, M. G. and Jang, I. S. (2013). The Tip of the Red Giant Branch Distances to Type Ia Supernova Host Galaxies. II. M66 and M96 in the Leo I Group. *ApJ*, **773**, 13.

Lefor, A. T., Futamase, T., and Akhlaghi, M. (2012). A Systematic Review of Strong Gravitational Lens Modeling Software. *arXiv:1206.4382*.

Lehar, J., Falco, E. E., Kochanek, C. S., McLeod, B. A., Munoz, J. A., Impey, C. D., Rix, H. W., Keeton, C. R., and Peng, C. Y. (2000). Hubble Space Telescope Observations of 10 Two-Image Gravitational Lenses. *ApJ*, **536**, 584–605.

Lidman, C., Courbin, F., Meylan, G., Broadhurst, T., Frye, B., and Welch, W. (1999). The Redshift of the Gravitationally Lensed Radio Source PKS 1830-211. *ApJ*, **514**, L57–L60.

Lovell, J., Reynolds, J., Jauncey, D., Backus, P., McCulloch, P., Sinclair, M., Wilson, W., Tzioumis, A., King, E., Gough, R., Ellingsen, S., Phillips, C., Preston, R., and Jones, D. (1996). PKS 1830-211: A Possible Compound Gravitational Lens. *ApJL*, **472**, L5.

Lovell, J. E. J., Jauncey, D. L., Reynolds, J. E., Wieringa, M. H., King, E. A., Tzioumis, A. K., McCulloch, P. M., and Edwards, P. G. (1998). The Time Delay in the Gravitational Lens PKS 1830-211. *ApJL*, **508**, L51–L54.

Mathur, S. and Nair, S. (1997). X-ray Absorption towards the Einstein Ring Source PKS 1830-211. *ApJ*, **484**, 140.

Muller, S. (2011). Absorption Line Surveys at Intermediate Redshift. In J. Cernicharo and R. Bachiller, editors, *IAU Symposium*, volume 280 of *IAU Symposium*, pages 339–350.

Muller, S. and Guélin, M. (2008). Drastic changes in the molecular absorption at redshift z = 0.89 toward the quasar PKS 1830-211. *A&A*, **491**, 739–746.

Muller, S., Guélin, M., Dumke, M., Lucas, R., and Combes, F. (2006). Probing isotopic ratios at z = 0.89: molecular line absorption in front of the quasar PKS 1830-211. *A&A*, **458**, 417–426.

Muller, S., Beelen, A., Guélin, M., Aalto, S., Black, J. H., Combes, F., Curran, S. J., Theule, P., and Longmore, S. N. (2011). Molecules at z = 0.89. A 4-mm-rest-frame absorption-line survey toward PKS 1830-211. *A&A*, **535**, A103.

Muller, S., Beelen, A., Black, J. H., Curran, S. J., Horellou, C., Aalto, S., Combes, F., Guélin, M., and Henkel, C. (2013). A precise and accurate determination of the cosmic microwave background temperature at z = 0.89. *A&A*, **551**, A109.

Nair, S., Narasimha, D., and Rao, A. P. (1993). PKS 1830-211 as a gravitationally lensed system. *ApJ*, **407**, 46–59.

Nair, S., Jin, C., and Garrett, M. A. (2005). Helical Jet in the Gravitationally Lensed Blazar PKS1830-211. *MNRAS*, **362**, 1157–1166.

Navarro, J. F., Frenk, C. S., and White, S. D. M. (1997). A Universal Density Profile from Hierarchical Clustering. *ApJ*, **490**, 493.

Oguri, M. (2007). Gravitational Lens Time Delays: A Statistical Assessment of Lens Model Dependences and Implications for the Global Hubble Constant. *ApJ*, **660**, 1–15.

Oguri, M. (2010). The Mass Distribution of SDSS J1004+4112 Revisited. *PASJ*, **62**, 1017–1024.

Oguri, M. and Marshall, P. J. (2010). Gravitationally lensed quasars and supernovae in future wide-field optical imaging surveys. *MNRAS*, **405**, 2579–2593.

Paraficz, D., Hjorth, J., and Elíasdóttir, Á. (2009). Results of optical monitoring of 5 SDSS double QSOs with the Nordic Optical Telescope. *A&A*, **499**, 395–408.

Patnaik, A. R., Muxlow, T. W. B., and Jauncey, D. L. (1993). MERLIN 5-GHz observations of PKS1830-211. In J. Surdej, D. Fraipont-Caro, E. Gosset, S. Refsdal, and M. Remy, editors, *Liege International Astrophysical Colloquia*, volume 31 of *Liege International Astrophysical Colloquia*, page 363.

Pence, W. (1999). CFITSIO, v2.0: A New Full-Featured Data Interface. In D. M. Mehringer, R. L. Plante, and D. A. Roberts, editors, *Astronomical Data Analysis Software and Systems VIII*, volume 172 of *Astronomical Society of the Pacific Conference Series*, page 487.

Phillips, R. B. and Mutel, R. L. (1982). On symmetric structure in compact radio sources. *A&A*, **106**, 21–24.

Planck Collaboration, Ade, P. A. R., Aghanim, N., Armitage-Caplan, C., Arnaud, M., Ashdown, M., Atrio-Barandela, F., Aumont, J., Baccigalupi, C., Banday, A. J., and et al. (2013). Planck 2013 results. XVI. Cosmological parameters. *ArXiv e-prints*.

Pramesh Rao, A. and Subrahmanyan, R. (1988). 1830-211 - A flat-spectrum radio source with double structure. *MNRAS*, **231**, 229–236.

Press, W. H., Teukolsky, S. A., Vetterling, W. T., and Flannery, B. P. (1992). *Numerical Recipes in C: The Art of Scientific Computing*. Cambridge University Press.

Refsdal, S. (1964). On the possibility of determining Hubble's parameter and the masses of galaxies from the gravitational lens effect. *MNRAS*, **128**, 307.

Sakai, S., Mould, J. R., Hughes, S. M. G., Huchra, J. P., Macri, L. M., Kennicutt, R. C., Gibson, B. K., Ferrarese, L., Freedman, W. L., Han, M., Ford, H. C., Graham, J. A., Illingworth, G. D., Kelson, D. D., Madore, B. F., Sebo, K., Silbermann, N. A., and Stetson, P. B. (2000). The Hubble Space Telescope Key Project on the Extragalactic Distance Scale. XXIV. The Calibration of Tully-Fisher Relations and the Value of the Hubble Constant. *ApJ*, **529**, 698–722.

Schneider, P. and Weiss, A. (1986). The two-point-mass lens - Detailed investigation of a special asymmetric gravitational lens. *A&A*, **164**, 237–259.

Schneider, P., Ehlers, J., and Falco, E. (1992). *Gravitational Lenses*. Springer-Verlag.

Schneider, P., Kochanek, C., and Wambsganss, J. (2006). *Gravitational Lensing: Strong, Weak and Micro*. Springer, Berlin.

Shimmins, A., Manchester, R. N., and Harris, B. J. (1969). Accurate Flux Densities at 5009 MHz of 753 Radio Sources. *Australian J. Phys. Suppl.*, **8**, 3.

Smith, R. J., Blakeslee, J. P., Lucey, J. R., and Tonry, J. (2005). Discovery of Strong Lensing by an Elliptical Galaxy at z = 0.0345. *ApJL*, **625**, L103–L106.

Subrahmanyan, R., Narasimha, D., Paramesh Rao, A., and Swarup, G. (1990). 1830-211: gravitationally lensed images of a flat-spectrum radio core? *MNRAS*, **246**, 263.

Suyu, S. H. (2012). Cosmography from two-image lens systems: overcoming the lens profile slope degeneracy. *MNRAS*, **426**, 868–879.

Suyu, S. H., Marshall, P. J., Hobson, M. P., and Blandford, R. D. (2006). A Bayesian analysis of regularized source inversions in gravitational lensing. *MNRAS*, **371**, 983–998.

Suyu, S. H., Marshall, P. J., Blandford, R. D., Fassnacht, C. D., Koopmans, L. V. E., McKean, J. P., and Treu, T. (2009). Dissecting the Gravitational Lens B1608+656. I. Lens Potential Reconstruction. *ApJ*, **691**, 277–298.

Suyu, S. H., Auger, M. W., Hilbert, S., Marshall, P. J., Tewes, M., Treu, T., Fassnacht, C. D., Koopmans, L. V. E., Sluse, D., Blandford, R. D., Courbin, F., and Meylan, G. (2013). Two Accurate Time-delay Distances from Strong Lensing: Implications for Cosmology. *ApJ*, **766**, 70.

Treu, T. and Koopmans, L. V. E. (2002). The internal structure of the lens PG1115+080: breaking degeneracies in the value of the Hubble constant. *MNRAS*, **337**, L6–L10.

Tully, R. B., Courtois, H. M., Dolphin, A. E., Fisher, J. R., Heraudeau, P., Jacobs, B. A., Karachentsev, I. D., Makarov, D., Makarova, L., Mitronova, S., Rizzi, L., Shaya, E. J., Sorce, J. G., and Wu, P.-F. (2013). Cosmicflows-2: The Data. *ArXiv e-prints*.

Turner, E. L., Ostriker, J. P., and Gott, III, J. R. (1984). The statistics of gravitational lenses - The distributions of image angular separations and lens redshifts. *ApJ*, **284**, 1–22.

van den Bosch, F. C., Abel, T., Croft, R. A. C., Hernquist, L., and White, S. D. M. (2002). The Angular Momentum of Gas in Protogalaxies. I. Implications for the Formation of Disk Galaxies. *ApJ*, **576**, 21–35.

van Ommen, T. D., Jones, D. L., Preston, R. A., and Jauncey, D. L. (1995). Time delay in the Einstein ring PKS 1830-211. *ApJ*, **444**, 561–566.

Vegetti, S., Lagattuta, D. J., McKean, J. P., Auger, M. W., Fassnacht, C. D., and Koopmans, L. V. E. (2012). Gravitational detection of a low-mass dark satellite galaxy at cosmological distance. *Nature*, **7381**, 341–343.

Vuissoz, C., Courbin, F., Sluse, D., Meylan, G., Ibrahimov, M., Asfandiyarov, I., Stoops, E., Eigenbrod, A., Le Guillou, L., van Winckel, H., and Magain, P. (2007). COSMOGRAIL: the COSmological MOnitoring of GRAvItational Lenses. V. The time delay in SDSS J1650+4251. *A&A*, **464**, 845–851.

Vuissoz, C., Courbin, F., Sluse, D., Meylan, G., Chantry, V., Eulaers, E., Morgan, C., Eyler, M. E., Kochanek, C. S., Coles, J., Saha, P., Magain, P., and Falco, E. E. (2008). COSMOGRAIL: the COSmological MOnitoring of GRAvItational Lenses. VII. Time delays and the Hubble constant from WFI J2033-4723. *A&A*, **488**, 481–490.

Walsh, D., Carswell, R. F., and Weymann, R. J. (1979). 0957 + 561 A, B - Twin quasistellar objects or gravitational lens. *Nature*, **279**, 381–384.

Wiklind, T. and Combes, F. (1996). The redshift of the gravitational lens of PKS1830-211 determined from molecular absorption lines. *Nature*, **379**, 139–141.

Wiklind, T. and Combes, F. (1998). The Complex Molecular Absorption Line System at z = 0.886 toward PKS 1830-211. *ApJ*, **500**, 129.

Wiklind, T. and Combes, F. (2001). Time delay of PKS 1830-211 Using Molecular Absorption Lines. *ASPC*, **237**, 155.

Winn, J. N., Kochanek, C. S., McLeod, B. A., Falco, E. E., Impey, C. D., and Rix, H. (2002). PKS 1830-211: A Face-on Spiral Galaxy Lens. *ApJ*, **575**, 103–110.

Witt, H. J., Mao, S., and Keeton, C. R. (2000). Analytic Time Delays and H_0 Estimates for Gravitational Lenses. *ApJ*, **544**, 98.

Wucknitz, O., Biggs, A. D., and Browne, I. W. A. (2004). Models for the lens and source of B0218+357: a LENSCLEAN approach to determine H_0. *MNRAS*, **349**, 14–30.

York, T., Jackson, N., Browne, I. W. A., Wucknitz, O., and Skelton, J. E. (2005). The Hubble constant from the gravitational lens CLASS B0218+357 using the Advanced Camera for Surveys. *MNRAS*, **357**, 124–134.

Appendix A

Strong lensing in an expanding universe[1]

Although the equations for gravitational lensing in chapter 2 were derived within the framework of Euclidean geometry, they can be used to model lensing in an expanding universe if the distances used in these equations are interpreted as the cosmological angular diameter distances. Angular diameter distance D_A between an object at redshift z and the observer is defined in terms of the transverse comoving distance D_M as

$$D_A = \frac{D_M}{1+z}. \tag{A.1}$$

The transverse comoving distance of an object at redshift z can in turn be written using the cosmological parameters as

$$D_M = \begin{cases} D_H \frac{1}{\sqrt{\Omega_k}} \sinh[\sqrt{\Omega_k} D_c/D_H] & \text{for } \Omega_k > 0 \\ D_c & \text{for } \Omega_k = 0 \\ D_H \frac{1}{\sqrt{\Omega_k}} \sin[\sqrt{\Omega_k} D_c/D_H] & \text{for } \Omega_k < 0 \end{cases} \tag{A.2}$$

where D_H is the Hubble distance defined as $D_H \equiv c/H_0$ and the line-of-sight comoving distance D_c is given as

$$D_c = \frac{c}{H_0} \int_0^z \frac{dz'}{\sqrt{\Omega_M(1+z)^3 + \Omega_k(1+z)^2 + \Omega_\Lambda}}. \tag{A.3}$$

In equations A.2 and A.3, H_0 is the Hubble constant, Ω_M, Ω_k and Ω_Λ are the cosmological density parameters for matter, curvature and dark energy respectively. For a flat universe, $\Omega_k = 0$ and hence the angular diameter distance becomes

$$D_A = \frac{c}{H_0(1+z)} \int_0^z \frac{dz'}{\sqrt{\Omega_M(1+z)^3 + \Omega_\Lambda}}. \tag{A.4}$$

In an expanding universe, when the distances are interpreted as angular diameter distances, it is incorrect to relate the lens-to-observer, lens-to-source and source-to-observer distances simply as $D_s = D_d + D_{ds}$ (see figure 2.1). The angular diameter distance between two objects at redshifts z_1 and z_2, for cosmologies with $\Omega_K \geq 0$, is

$$D_{A12} = \frac{1}{1+z_2} \left(D_{M2} \sqrt{1 + \Omega_K \frac{D_{M1}^2}{D_H^2}} - D_{M1} \sqrt{1 + \Omega_K \frac{D_{M2}^2}{D_H^2}} \right) \tag{A.5}$$

where D_{M1} and D_{M2} are the transverse comoving distances to the two objects at z_1 and z_2 as defined in equation A.2.

[1] This section makes use of equations from Hogg (1999).

Appendix B

GRAVLENS

GRAVLENS was written by Charles R. Keeton originally for the **C**fA-**A**rizona **S**pace **T**elescope **LE**ns **S**urvey (CASTLES). The algorithm used to solve the lens equation and the techniques used to constrain a lens model are presented in Keeton (2001). In this section, only the relevant aspects of GRAVLENS are discussed; a detailed manual of the software package can be downloaded from the software's homepage[1].

GRAVLENS contains two standalone applications: *gravlens* and *lensmodel*. All basic features required to perform lens modelling is built in *gravlens* and it forms the backbone of the software package. More elaborate techniques used to constrain the modelled lens are included in *lensmodel* which is built on top of *gravlens*. Both applications are controlled using a set of variables and commands which can be given as input either individually in the application's user-interface, or can be specified in a text file which can then be parsed to the applications as a whole. Behaviour of each command in turn is governed by a set of mandatory and optional parameters.

The applications contain a rudimentary documentation for all commands which can be accessed by executing

`help` ⟨`command`⟩

Most of the variables used in both applications are set to a certain default value and the value of a particular variable can be displayed using the command

`set [variable]`

The square brackets indicate that that parameter is optional and if no variable is specified, a list of all variables with their default values is printed on the screen. To change the value of a given variable, the above command can be modified as

`set` ⟨`variable`⟩ `=` ⟨`value`⟩

As GRAVLENS uses the tiling method (see section 2.3.1) to solve the lens equation, the first step is to specify the resolution of the grid to be laid on the source and the image plane. The variables used to specify the tiling of the source and the image plane is listed in table B.1. Once those variables are set, a polar grid centered on the main lens galaxy is laid. In order to improve the resolution of the grid near important locations like the critical lines and images, *gravlens* uses recursive subgridding. The number of recursions near these points are specified using the variable 'maxlev' and 'imglev'.

The next step is to specify the type of mass model to define the lens. A list of all mass models supported by GRAVLENS can be obtained using the command 'listmodels'. The syntax for defining the lens is as follows:

[1] http://redfive.rutgers.edu/ keeton/gravlens/

Table B.1: Variables used to define the tiling of the source and the image plane

Variable	Description
gridlo1 gridhi1	Lower and upper values of the radial extent of the grid
gridlo2 gridhi2	Lower and upper values of the angular extent of the grid (measured in degrees East of North)

Table B.2: Parameters used in canonical mass models

Parameter	Description
[1]	Mass scale of the lens
[2,3]	Lens position
[4,5]	Ellipticity and position angle of the lens
[6,7]	External shear parameters (γ, θ_γ)
[8,9]	Scale radii (not used for all mass models)
[10]	Power law index (not used for all mass models)

```
setlens ⟨# of galaxies in each model⟩ ⟨# of mass models⟩
   ⟨Type for model #1, galaxy #1⟩
   ⟨Type for model #1, galaxy #n⟩
   ⋮
   ⟨Type for model #m, galaxy #1⟩
   ⟨Type for model #m, galaxy #n⟩
   ⟨Flags for model #1, galaxy#1⟩
   ⋮
   ⟨Flags for model #m, galaxt #n⟩
```

In the above syntax, it is easy to spot the slightly confusing terminology that GRAVLENS uses to refer to individual components of a lensing system. GRAVLENS uses the term "mass models" to refer to each physical galaxy and the term "galaxy" to refer to mass distributions like SIS or NFW that are used to describe each component of a physical galaxy. For example, if the lens is made of two spiral galaxies and if each spiral galaxy is modelled as a combination of three components (disk, bulge and halo), then the first line of the syntax must be written as

```
setlens 3 2
```

GRAVLENS uses 10 parameters to define the type of each mass distribution and explanation for each parameter can be found in table B.2. The last three parameters are not used by all mass models but they must still be specified in the code. The use of 'Flags' varies between the two applications: *gravlens* does not use these values and hence all 10 flags must be set to zero. Flags play a very important role in *lensmodel* and will be discussed later.

With this information, a number of basic lensing calculations can be performed. For example, consider a gravitational lens system whose lens is described as a singular isothermal sphere (SIS) with a one dimensional velocity dispersion of 188 km/s. Let the source and lens redshift be 2.5 and 0.89 respectively. For such a lens configuration, the critical lines and caustics can be generated using the command

```
plotcrit ⟨output_filename⟩
```

Similarly, the grid used to tile both planes can be displayed using the command

`plotgrid ⟨output_filename⟩`

The critical lines and caustics along with the grid for this lens model are shown in figure B.1. It should be noted that the applications themselves do not generate any graphical output; instead the output is provided in the form of data files which can then be used to produce graphical output using any plotting software like gnuplot or MATLAB. Each data file contains a list of instructions on how it can be used to generate plots.

GRAVLENS also allows to find the total number of images, the magnification and the position of each image for a given unlensed source position (u,v). This is achieved using the command

`findimg ⟨u⟩ ⟨v⟩`

Two other commands - *findimg2* and *findimg3* - have the same functionality as findimg, except for the way in which they handle the input and output. *findimg2* facilitates specifying a series of source positions for each of which the application finds the corresponding number of images and their source position. *findimg3* can read a series of source positions specified in an input file and writes the corresponding results to an output file.

Instead of using point sources, it is also possible to specify complex source models using three basic building blocks defined in the code: point sources, sources with constant surface brightness and sources with a Sersic brightness profile. The syntax used to specify a source model is

```
setsource ⟨# of sources⟩
   ⟨Type of source #1⟩
   ⋮
   ⟨Type of source #n⟩
```

Once a source model is specified, the *SBmap2* command can be used to generate the lensed surface brightness map of the specified source. A simple source and its lensed image are displayed in figure B.2. The source is modelled as the sum of a central component with uniform surface brightness to represent the core and an extended, two dimensional ellipsoidal component with a Sersic profile to represent a jet.

Apart from calculating the positions of the images and generating the lensed surface brightness maps, GRAVLENS can also be used to find the best model that fits the specified observational constraints. GRAVLENS finds the best fit for the specified observational data in the following way: for a given mass distribution, the code varies each free parameter and for each configuration of free parameters, the code simulates the observables which are then used along with the specified observational constraints to compute the χ^2 values. Then, the code identifies the parameters that produce the least χ^2 as the best fit model. This is done by the application *lensmodel* and since *lensmodel* is built on top of *gravlens*, all the commands and variables discussed so far are valid within *lensmodel* as well. The first step in doing model fitting using *lensmodel* is to give the observational constraints in a separate file. This file can then be loaded into *lensmodel* using the command

`data ⟨Data File⟩`

Once the observational constraints are specified, the next step is to define the lens model and the syntax is exactly the same as what was used for *gravlens*. The only difference is that *lensmodel* takes the flags into account whereas *gravlens* ignores them even though they must be written down. If a particular model parameter is to be allowed to float freely, the corresponding '**vary flag**' is set to '1'.

Finally, the three most important commands that are used to produce the best fit model are *varyone*, *varytwo* and *optimize*. As the names suggest, the first two commands are used

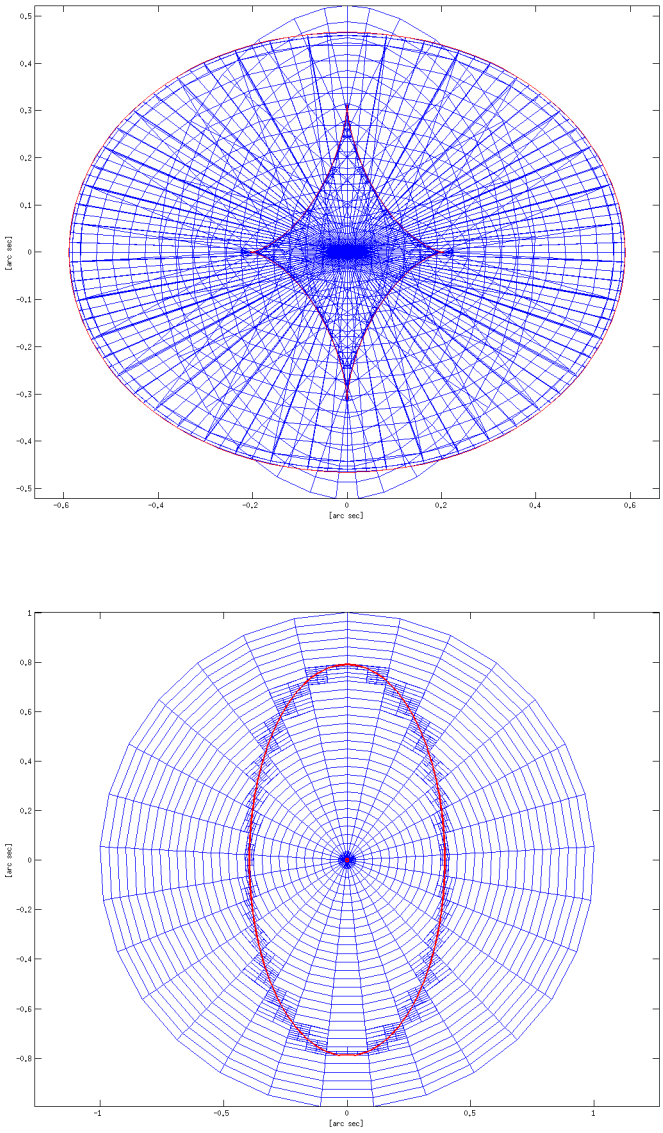

Figure B.1: Source plane and image planes for a singular isothermal ellipsoid with ellipticity 0.5 and position angle 0°. *Top*: Source plane grid (blue) with the two caustics (red). *Bottom*: Image plane grid (blue) with the two critical lines (red). Three levels of recursive subgridding can be seen along the critical lines.

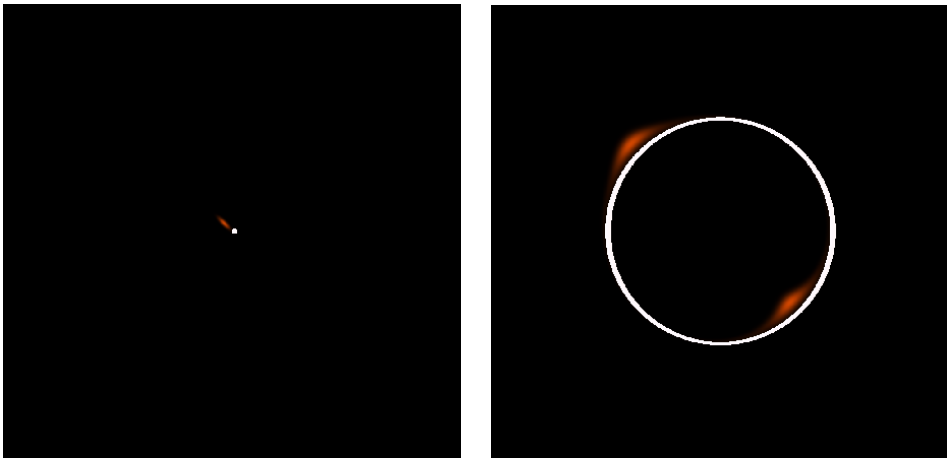

Figure B.2: *Left*: Surface brightness map of a source built using a uniform two dimensional ellipsoidal model and a Sersic brightness distribution. *Right*: Surface brightness map after lensing by an SIS mass model. The source is located exactly behind the lens, and it is lensed into an Einstein ring. The second component is lensed into two images.

to vary either a single or two free parameters within a specified range and for each interval the χ^2 values are computed. These two commands are used to obtain a first guess as to where the global χ^2 minimum is present in the parameter space. Once that is identified, the final refinement is done using *optimize*. Apart from computing the total χ^2, the application also outputs the χ^2 for different observational constraints (i.e. position, flux, and time delay). These values are computed using the simple statistic defined as Keeton (2001):

Position χ^2:

$$\chi^2_{position} = \sum_i \delta \boldsymbol{x}_i^T \cdot S_i^{-1} \cdot \delta \boldsymbol{x}_i \tag{B.1}$$

$$\delta \boldsymbol{x}_i = \boldsymbol{x}_{obs,i} - \boldsymbol{x}_{mod,i} \tag{B.2}$$

where $\boldsymbol{x}_{obs,i}$ and $\boldsymbol{x}_{mod,i}$ are the observed and modelled positions of the i^{th} image. The covariance matrix S_i is

$$S_i = R_i^T \begin{pmatrix} \sigma_{1,i}^2 & 0 \\ 0 & \sigma_{2,i}^2 \end{pmatrix} R_i \tag{B.3}$$

where

$$R_i = \begin{pmatrix} -sin\theta_{\sigma,i} & cos\theta_{\sigma,i} \\ -cos\theta_{\sigma,i} & -sin\theta_{\sigma,i} \end{pmatrix} \tag{B.4}$$

where $\sigma_{1,i}$ and $\sigma_{2,i}$ measure the error ellipses and $\theta_{\sigma,i}$ represents the position angle.

Flux χ^2:

$$\chi^2_{flux} = \sum_i \left(\frac{f_i - M_i f_{src}}{\sigma_{f,i}} \right)^2 \tag{B.5}$$

where $f_i \pm \sigma_{f,i}$ is the observed flux of the i^{th} image, M_i is the magnification of the i^{th} image and the f_{src} is the intrinsic source flux.

χ^2 contribution due to time delay:

$$\chi^2_{tdel} = \sum_i \left(\frac{\tau_{obs,i} - h^{-1} t_0 \bar{\tau}_{mod,i}}{\sigma_{t,i}} \right)^2 \tag{B.6}$$

where

$$t_0 = \frac{1+z_l}{c}\frac{D_{ol}D_{os}}{D_{ls}} \tag{B.7}$$

$$\bar{\tau}_{mod,i} = \frac{1}{2}\left(|\boldsymbol{x}_i - \boldsymbol{u}|^2 - |\boldsymbol{x}_{lead} - \boldsymbol{u}|^2\right) - (\phi(\boldsymbol{x}_i) - \phi(\boldsymbol{x}_{lead})) \tag{B.8}$$

where $\boldsymbol{x}_i$ and $\boldsymbol{x}_{lead}$ are the image plane positions of the i^{th} image and the "leading" image respectively. $\boldsymbol{u}$ is the unlensed source position and ϕ is the potential of the lens mass distribution.

The three above mentioned commands produce different outputs that are saved under files with different file extensions. The bestfit model (that has the least χ^2) is stored under a file with extension '.best' and a summary of the results for each interval in the specified parameter range is stored in a '.dat' file.

Performing model fitting using *lensmodel* is demonstrated in appendix C by replicating the results published in Winn *et al.* (2002).

Appendix C

Replicating Winn *et al.* (2002)

For the sake of better understanding and to demonstrate our ability to use GRAVLENS, we replicate in this section the results of Winn *et al.* (2002) who model PKS 1830-211 using a singular isothermal ellipsoidal lens (a brief discussion of the results of Winn *et al.* is presented in §4.1.1). The observational constraints used in Winn *et al.* (2002) are shown in table C and the data file where these values are described is shown below:

```
1 # No. of lens
0.328 -0.486 0.004 # Lens position with error
0.5 1000
0.0 1e4 # Position angle of the lens
0.0 1e4 # Lens ellipticity

1 # No. of sources
2 # No. of images produced

#xpos ypos flux pos_error flux_error delay delay_error
0 0 1.52 0.001 0.05 0 4 # NE image
0.642 -0.728 -1.0 0.001 0.05 26 4 # SW image
```

Note that the error bars on the observed values of lens ellipticity, lens orientation are very high in order to force the code not to use them as constraints. Once the constraints are declared, the next step is to define the lens model to be used. This is done exactly the same way as in *gravlens* except that the flags are taken into consideration in *lensmodel*. Since we are fitting an SIE lens, the free parameters are mass of the lens, lens ellipticity and position angle. Therefore the lens is described as

```
setlens 1 1
```

Parameter	**Value**
NE image	(0",0")
SW image	(0".642,-0".728)±0".001
Lens position	(0".328,-0".486)±0".004
Flux ratio (NE/SW)	1.52±0.05
Time delay (SW - NE)	26^{+4}_{-5} days
Lens redshift	0.886±0.001
Source redshift	2.507±0.002

Table C.1: Observational constraints used in Winn *et al.* (2002)

```
alpha 1.0 0.328 -0.486 0.1 10.0 0 0 0 0 1.0
1 0 0 1 1 0 0 0 0 0
```

As explained earlier, in order to identify the region of the parameter space that might contain the global χ^2 minimum, we first generate a two dimensional grid by varying the lens ellipticity and lens orientation from 0.0 to 0.5 and from 0° to 180° respectively. This is implemented using the command

```
varytwo 1 4 0.0 0.5 25 1 5 0 180 25 vary_e_pa
```

This command instructs *lensmodel* to vary the 4^{th} and the 5^{th} parameters (ellipticity and position angle) of the 1^{st} 'galaxy', compute the χ^2 for each of the combination and write the output to the file specified at the end of the line. Once this is done, the fit can be refined using the command 'optimize'. The complete *lensmodel* script used to perform model fitting is appended below:

```
set omitcore = 0.05 # core radius to avoid the singularity at r = 0
set nobflip = 1

# First choose source plane chisq
set chimode = 0 # 0 - source plane chi
set gridflag = 0
set checkparity = 0

# Load the data file
data Winn.et.al.data

# Cosmology
set lambda = 0.7
set omega = 0.3
set hval = 0.5
# A large uncertainty on H0 prevents the code from using it as a constraint
set hvale = 1E6

set zsrc = 2.507
set zlens = 0.889

setlens 1 1
alpha 1.0 0.328 -0.486 0.1 10.0 0 0 0 0 1.0
1 0 0 1 1 0 0 0 0 0

varytwo 1 4 0.0 0.5 25 1 5 0 180 25 vary_e_pa

setlens vary_e_pa.start

optimize srcPlane

# Switch to image plane statistic
set gridflag = 1
set chimode = 1
set checkparity = 1
```

Table C.2: Comparison between the results produced in Winn *et al.* (2002) and the analysis replicated in this section.

Parameters	**Winn *et al.***	**Replicated results**
Einstein ring radius	0".491±0".001	0".491±0".0004
Ellipticity	0.091±0.009	0.0917±0.005
Lens orientation	86.1±3.1	86.17°±1.2°
Unlensed source position	(0".264,-0".418)±0.005	(0".264,-0".418)
Magnification of NE	5.9±0.6	5.81±0.4
Hubble constant	44±9	44.14±2.5

```
setlens srcPlane.start

optimize

quit
```

The above script, in its entirety, works in the following way: The cosmological parameters are set and the observational data files are loaded. *lensmodel* is instructed to avoid the demagnified third image using the 'omitcore' variable; the 'nobflip' variable forces the value of Einstein's radius to remain positive. When the mass distribution for the lens is specified, Einstein ring radius, lens ellipticity and position angle are allowed to vary. Note that the first optimization is done using the source plane χ^2 and then the parameters are refined using the image plane χ^2 to identify the best fit model. The results of our analysis along with the ones produced by Winn *et al.* (2002) are shown in table C.2.

Appendix D

Single lens model fitting of PKS 1830-211: Results

Results from the single lens model fitting discussed in section §4.2 is presented in this appendix. Table D.1 lists the two sets of observational data used to constrain the lens model and the results from those model fitting runs are shown in Tables D.2 – D.5. For a detailed discussion of the model fitting procedure, refer to the text on page 23.

Table D.1: Observational constraints for the lens model. All positions are measured with respect to the NE image.

Constraints	**Value**	**Reference**
NE Image	(0,0)	
SW Image	(0".642, -0".728)±0.001	Jin *et al.* (1999)
Lens position W	(0".328, -0".486)±0.004	Winn *et al.* (2002)
Lens position G	(0".519, -0".511)±0.08	Courbin *et al.* (2002)
Lens position SP	(0".285, -0".722)±0.04	Courbin *et al.* (2002)
Lens position SA	(0".3, -0".61)±0.05	Courbin *et al.* (2002)
Old flux ratio (NE/SW)	1.52±0.05	Lovell *et al.* (1998)
New flux ratio (NE/SW)	1.35±0.14	Muller et al (Private communication)
Old time delay (SW - NE)	26±4 days	Lovell *et al.* (1998)
New time delay (SW - NE)	27.1±0.6 days	Barnacka *et al.* (2011)
Hubble constant	70.2±2.2 km/s/Mpc	Hinshaw *et al.* (2012)

Table D.2: Results from model fitting for single mass models with lens positioned at W and constraints from old observations.

		SIE$_{old}$	**SIE**$_{old}$+**H**$_0$	**SIE**$_{new}$	**SIE**$_{new}$+**H**$_0$
Observational	Lens position	(0".328,-0".486)±0.004	(0".328,-0".486)±0.004	(0".328,-0".486)±0.004	(0".328,-0".486)±0.004
constraints	NE Image	(0,0)	(0,0)	(0,0)	(0,0)
	SW Image	(0".642,-0".728)±0.001	(0".642,-0".728)±0.001	(0".642,-0".728)±0.001	(0".642,-0".728)±0.001
	Flux ratio	1.52±0.05	1.52±0.05	1.35±0.14	1.35±0.14
	Time delay	26±4	26±4	27.1±0.6	27.1±0.6
	H_0		70.0±2.2		70.0±2.2
Best fit	Source position	(0".264,-0".418)	(0".264,-0".418)	(0".272, -0".430)	(0".264, -0".416)
	$f_{NE/source}$	5.81	5.81	6.85	5.43
	Einstein radius	0".491	0".491	0".506	0".489
	h	0.4425	0.6966	0.374	0.5966
	e	0.091	0.092	0.089	0.094
	PA	86.19	86.19	84.91°	-87.98°
Degrees of Freedom		0	1	0	1
Model values	NE Image	(0.0,0.0)	(-0".0,-0".0)	(0,0)	(-0".0007, 0".0011)
	SW Image	(0.642,-0.728)	(0.642,-0.728)	(0".675,-0".729)	(0".6413,-0".7275)
	NE flux	1.52	1.52	1.52	1.35
	SW flux	-1.0	-1.0	-1.0	-1.0
	$t_{SW} - t_{NE}$	26 days	16.52 days	27.1 days	19.51 days
χ^2					
Total		$7.5*10^{-10}$	2.83	$5.4*10^{-10}$	112.75
Position		$1.44*10^{-10}$	0.00138	$5.33*10^{-10}$	2.38
Flux		$6.07*10^{-10}$	$4.32*10^{-10}$	$7.36*10^{-10}$	$2.69*10^{-8}$
Time delay		$1.66*10^{-13}$	2.83	$3.18*10^{-13}$	110

Table D.3: Results from model fitting for single mass models with lens positioned at G.

		SIE$_{old}$	**SIE**$_{old}$+**H**$_0$	**SIE**$_{new}$	**SIE**$_{new}$+**H**$_0$
Observational	Lens position	(0".519,-0".511)±0.08	(0".519,-0".511)±0.08	(0".519,-0".511)±0.08	(0".519,-0".511)±0.08
constraints	NE Image	(0,0)	(0,0)	(0,0)	(0,0)
	SW Image	(0".642,-0".728)±0.001	(0".642,-0".728)±0.001	(0".642,-0".728)±0.003	(0".642,-0".728)±0.003
	Flux ratio	1.52±0.05	1.52±0.05	1.35±0.14	1.35±0.14
	Time delay	26±4	26±4	27.1±0.6	27.1±0.6
	H_0		70.0±2.2		70.0±2.2
Best fit	Source position	(0".366,-0".330)	(0".366,-0".330)	(0".365, -0".330)	(0".365, -0".331)
	$f_{NE/source}$	2.22	2.22	2.14	2.14
	Einstein radius	0".457	0".457	0".451	0".451
	h	1.11	0.7131	1.065	0.9197
	e	0.298	0.298	0.328	0.328
	PA	-31.66	-31.66	-33.89°	-33.85°
Degrees of Freedom		0	1	0	1
Model values	NE Image	(0.0,0.0)	(-0".0,-0".0)	(0,0)	(0".0004, -0".0004)
	SW Image	(0.642,-0.728)	(0.642,-0.728)	(0".642,-0".728)	(0".6421,-0".7282)
	NE flux	1.52	1.52	1.35	1.35
	SW flux	-1.0	-1.0	-1.0	-1.0
	$t_{SW} - t_{NE}$	26 days	40.5 days	27.1 days	31.3 days
χ^2					
Total		4.03*10^{-9}	6.89	9.63*10^{-10}	82.99
Position		5.35*10^{-19}	0.00363	8.08*10^{-10}	0.368
Flux		2.87*10^{-19}	3.61*10^{-9}	1.55*10^{-11}	1.90*10^{-6}
Time delay		6.69*10^{-14}	6.89	5.76*10^{-14}	82.63

Table D.4: Results from model fitting for single mass models with lens positioned at SP.

		SIE$_{old}$	**SIE**$_{old}$+**H**$_0$	**SIE**$_{new}$	**SIE**$_{new}$+**H**$_0$
Observational	Lens position	(0".285,-0".722)±0.04	(0".285,-0".722)±0.04	(0".285,-0".722)±0.04	(0".285,-0".722)±0.04
constraints	NE Image	(0,0)	(0,0)	(0,0)	(0,0)
	SW Image	(0".642,-0".728)±0.001	(0".642,-0".728)±0.001	(0".642,-0".728)±0.003	(0".642,-0".728)±0.001
	Flux ratio	1.52±0.05	1.52±0.05	1.35±0.14	1.35±0.14
	Time delay	26±4	26±4	27.1±0.6	27.1±0.6
	H_0		70.0±2.2		70.0±2.2
Best fit	Source position	(0".180,-0".587)	(0".180,-0".587)	(0".180, -0".587)	(0".188, -0".587)
	$f_{NE/source}$	1.74	1.74	1.68	1.68
	Einstein radius	0".465	0".465	0".465	0".465
	h	1.136	0.7142	1.089	0.9362
	e	0.618	0.618	0.61	0.61
	PA	-77.34	-77.35	-77.33°	-77.35°
Degrees of Freedom		0	1	0	1
Model values	NE Image	(-0.0123,-0.0040)	(-0".0123,-0".0041)	(0.0124,-0.0040)	(-0".0122, -0".0046)
	SW Image	(0.6372,-0.7553)	(0.6372,-0.7553)	(0".6370,-0".7552)	(0".6373,-0".7553)
	NE flux	1.62	1.62	1.4806	1.48
	SW flux	-0.8	-0.8	-0.74	-0.73
	$t_{SW} - t_{NE}$	26 days	40.5 days	27.1 days	31.5 days
χ^2					
Total		955.9	963.65	941.48	1032.9
Position		937.16	937.16	937.1	937
Flux		18.75	18.74	4.37	4.34
Time delay		7.21*10^{-14}	7.74	6.27*10^{-14}	90.97

Table D.5: Results from model fitting for single mass models with lens positioned at SA.

		SIE$_{old}$	**SIE**$_{old}$+**H**$_0$	**SIE**$_{new}$	**SIE**$_{new}$+**H**$_0$
Observational	Lens position	(0".3,-0".61)±0.05	(0".3,-0".61)±0.05	(0".3,-0".61)±0.05	(0".3,-0".61)±0.05
constraints	NE Image	(0,0)	(0,0)	(0,0)	(0,0)
	SW Image	(0".642,-0".728)±0.001	(0".642,-0".728)±0.001	(0".642,-0".728)±0.001	(0".642,-0".728)±0.001
	Flux ratio	1.52±0.05	1.52±0.05	1.35±0.14	1.35±0.14
	Time delay	26±4	26±4	27.1±0.6	27.1±0.6
	H_0		70.0±2.2		70.0±2.2
Best fit	Source position	(0".202,-0".504)	(0".202,-0".504)	(0".205, -0".500)	(0".205, -0".500)
	$f_{NE/source}$	2.66	2.66	2.56	2.56
	Einstein radius	0".492	0".492	0".487	0".487
	h	0.7854	0.7020	0.754	0.7276
	e	0.368	0.368	0.377	0.37
	PA	-0.8196	-0.8196	-79.35°	-79.36°
Degrees of Freedom		0	1	0	1
Model values	NE Image	(0.0,0.0)	(-0".0,-0".0)	(0.0,-0.0)	(-0".0, 0".0)
	SW Image	(0.642,-0.728)	(0.642,-0.728)	(0".642,-0".728)	(0".6421, -0".7280)
	NE flux	1.52	1.52	1.35	1.35
	SW flux	-1.0	-1.0	-1.0	-1.0
	$t_{SW} - t_{NE}$	26 days	29.1 days	27.1 days	28.04 days
χ^2					
Total		$9.57*10^{-10}$	0.306	$9.75*10^{-10}$	2.73
Position		$9.55*10^{-10}$	$1.71*10^{-4}$	$8.78*10^{-10}$	0.029
Flux		$1.19*10^{-12}$	$5.18*10^{-11}$	$9.74*10^{-11}$	$2.16*10^{-08}$
Time delay		$5.8*10^{-15}$	0.3066	$2.48*10^{-15}$	2.69

Appendix E

Lens modelling through mock simulations

As noted in section §5.2, images of extended sources provide better constraints for modelling the lens than point sources. In this section, we briefly explain the code that was written as a part of this thesis to identify the source and the lens structure that reproduces the observed extended features best.

As explained already, the essential idea behind the code is to simulate a large number of mock observations for different combinations of lens and source parameters within the defined parameter space, and then identify the best source-lens configuration by comparing the simulated images with the observed image. The range of parameters for both the lens and the source are defined in two separate files whose format is given below. In the current version of the code, only a singular isothermal ellipsoid lens mass distribution and a sersic profile for the source brightness distribution have been implemented. More models for the lens and the source will be added with time.

Each lens model is defined by a set of six numbers – lens mass, lens position, lens ellipticity and position angle, and power law index – and the structure for the lens file is

```
[No. of lens models]

[For each lens model:]
[mass (min)] [mass (max)]
[xpos (min)] [xpos (max)]
[ypos (min)] [ypos (max)]
[e    (min)] [e    (max)]
[PA   (min)] [PA   (max)]
[α    (min)] [α    (min)]
```

In the case of the source, seven parameters – intrinsic source flux, unlensed source position, source ellipticity and position angle, half light radius of the source, and source sersic index – are used to define a single source component and the structure of the source file is

```
[No. of source components]

[For each source component:]
[flux (min)] [flux (max)]
[xpos (min)] [xpos (max)]
[ypos (min)] [ypos (max)]
[e    (min)] [e    (max)]
[PA   (min)] [PA   (max)]
```

```
[R    (min)] [R    (max)]
[n    (min)] [n    (min)]
```

For a given number of intervals, the code generates all possible lens-source configurations and generates parameter files which are then executed using *gravlens* to produce the simulated image. Once all the images are generated, the code then compares the generated images with the observed image and identifies the best fit model using a simple χ^2 statistic. FITS images are maniputed using the functions provided by the CFITSIO library (Pence, 1999) and numerical integrations required in the code are performed using the GNU Scientific Library (GSL)[1]. Though the code is very expensive in terms of memory usage[2] and computation time, the code results in a better lens model than what is produced by point images.

[1] `https://www.gnu.org/software/gsl/`

[2] Memory usage can be reduced significantly by making minor modifications to the existing code.

Appendix F

Previous H_0 estimates

Table F.1: Previous H_0 estimates using gravitationally lensed quasars.

		Cosmology			
Quasar	$\boldsymbol{H_0}$	**A/D**^{II}	$\boldsymbol{\Omega_m}$	$\boldsymbol{\Omega_\Lambda}$	**Reference**
SDSS J1650+4251	$51.7^{+4.0}_{-3.0}$	A	0.3	0.7	(a)^I
WFI J2033-4723 (non-parametric)	67^{+13}_{-10}	–	–	–	(b)^I
WFI J2033-4723 (SIS model)	63^{+7}_{-3}	–	–	–	(b)^I
RXJ 1131-1231 + WMAP	$80^{+5.8}_{-5.7}$	D	–	0.79 ± 0.03	(c)^I
RXJ 1131-1231 and B1608+656 + WMAP	$75.2^{+4.4}_{-4.2}$	D	–	$0.76^{+0.02}_{-0.03}$	(c)^I
B0218+357	78 ± 6	A	0.3	0.7	(d)
	70 ± 5	A	0.27	0.73	(e)
	61 ± 7	A	0.27	0.73	(e)
FBQ0951+2635	$60^{+9}_{-7} \pm 2$	A	0.3	0.7	(f)
Q0957+561	77^{+29}_{-24}	–	–	–	(g)
PG 1115+080	$59^{+12}_{-7} \pm 3$	A	0.3	0.7	(h)
SDSS J1206+4332	73^{+3}_{-4}	A	0.3	0.7	(i)
SBS 1520+530	51 ± 9	A	0.3	0.7	(j)
B1600+434	52^{+14}_{-8}	A	0.3	0.0	(k)
B1608+656	75^{+7}_{-6}	A	0.3	0.7	(l)
HE 2149-2745	$66 \pm 8 \pm 6$	A	0.3	0.7	(m)

References: a. Vuissoz *et al.* (2007); b. Vuissoz *et al.* (2008); c. Suyu *et al.* (2013); d. Wucknitz *et al.* (2004); e. York *et al.* (2005); f. Jakobsson *et al.* (2005); g. Bernstein and Fischer (1999); h. Treu and Koopmans (2002); i. Paraficz *et al.* (2009); j. Burud *et al.* (2002b); k. Burud *et al.* (2000); l. Koopmans *et al.* (2003); m. Burud *et al.* (2002a)

Notes: I. Part of the COSMOGRAIL project.

II. 'A' and 'D' stand for assumed and derived cosmological parameters respectively.

Table F.2: Recent estimations of Hubble constant using different cosmological probes. All measurements are obtained assuming a flat ΛCDM cosmological model.

			Cosmology			
S. No.	**Description**	$\boldsymbol{H_0}$	**A/D**^{I} I	$\boldsymbol{\Omega_m}$	$\boldsymbol{\Omega_\Lambda}$	**Reference**
1.	Hubble Key Science Project:			Model independent		(1)
	– Type Ia SNe	$71 \pm 2 \pm 6$				
	– TF relation	$71 \pm 3 \pm 7$				
	– SB fluctuation	$70 \pm 5 \pm 6$				
	– Type II SNe	$72 \pm 9 \pm 7$				
	– Fundamental plane	$82 \pm 6 \pm 9$				
	– Combined	72 ± 8				
2.	Wilkinson Microwave Anisotropy Probe (WMAP):					(2)
	– WMAP9 only	70.0 ± 2.2	D	0.279 ± 0.025	0.721 ± 0.025	
	– WMAP9 + BAO	68.65 ± 0.93	D	0.295 ± 0.011	0.705 ± 0.011	
3.	Planck satellite:					(3)
	– Planck only	67.4 ± 1.4	D	0.314 ± 0.020	0.686 ± 0.020	
	– Planck + Lensing	67.9 ± 1.5	D	0.307 ± 0.019	0.693 ± 0.019	
	– Planck + WP	67.3 ± 1.2	D	$0.315^{+0.016}_{-0.018}$	$0.685^{+0.018}_{-0.016}$	
	– Planck + WP + highL	67.3 ± 1.2	D	–	$0.685^{+0.017}_{-0.016}$	
	– Planck + lensing + WP + highL	67.9 ± 1.0	D	–	0.693 ± 0.013	
	– Planck + WP + highL + BAO	67.8 ± 0.77	D	–	0.692 ± 0.010	
4.	Megamaser Cosmology Project	68.0 ± 4.8		Model independent		(4)
5.	Baryon Oscillation Spectroscopic Survey	$90.8 \pm 6.2^{\mathrm{I}}$	–	–	–	(5)
6.	Cosmic Flows-2	74.4 ± 3.0		Model independent		(6)
7.	Tip of the Red Giant Branch (TRGB) method	$68.4 \pm 2.6 \pm 3.7$		Model independent		(7)
8.	The Carnegie Hubble Program	74.3 ± 2.1		Model independent		(8)
9.	The 6dF Galaxy Survey	67 ± 3.2		Model independent		(9)
10.	WiggleZ Dark Energy Survey:		–	–	–	(10)
	– $z = 0.44$	82.6 ± 7.8				
	– $z = 0.6$	87.9 ± 6.1				
	– $z = 0.73$	97.3 ± 7.0				

References: 1. Freedman *et al.* (2001); 2. Hinshaw *et al.* (2012); 3. Planck Collaboration *et al.* (2013); 4. Braatz *et al.* (2013); 5. Kazin *et al.* (2013); 6. Tully *et al.* (2013); 7. Lee and Jang (2013); 8. Freedman *et al.* (2012); 9. Colless *et al.* (2013); 10. Blake *et al.* (2012);

Notes: I. Given value is for $z = 0.57$.

II. 'A' and 'D' stand for assumed and derived cosmological parameters respectively.

Appendix G

Magnification map for a 2-point mass lens

The MATLAB code used to generate the magnification maps for a 2-point mass lens is presented in this appendix. The lens model and the cosmological model are defined in functions *modelParam* and *cosmoParam* respectively. The main code is written in the file *Code.m*. This MATLAB code can be extended to generate magnification maps for any canonical mass distribution with very little modification to the code in the file *Code.m*. See appendix H for the MATLAB code to generate the magnification maps for a double SIS lens.

```
% ------------------------------------------------------------------------
%
%   Name: Code.m
%
%   Purpose:
%   Code to simulate the magnification maps due to a 2-point mass lens
%
%   Reference:  Schneider & Weiss (1986)
%
% ------------------------------------------------------------------------

clear all;

model = modelParam();
cosmo = cosmoParam();

% 2D Identity matrix
I_2D = [1 0; 0 1];

% ------------------------------------------------------------------------
% Check for the validity of the input parameters
% ------------------------------------------------------------------------
flag = checkModel();

if flag == 1
    disp('Incorrect model parameters. Execution terminated!!!');
else
    disp('Input parameters verified. Proceeding to build the model');

% ------------------------------------------------------------------------
% Compute the required cosmological distances
% ------------------------------------------------------------------------
    disp('Computing the cosmological distances');
    %   Observer-to-lens
    D_d = getCoMovDist(model.z_lens)/(1+model.z_lens);

    %   Observer-to-source
    D_s = getCoMovDist(model.z_source)/(1+model.z_source);

    %   lens-to-source
    D_ds = (getCoMovDist(model.z_source) - getCoMovDist(model.z_lens))/(1+model.↙
z_source);

    % Critical surface mass density
    critDensity = ((cosmo.c^2)/(4*pi*cosmo.G)) * (D_s/(D_ds * D_d));

    % Create matrices for the Jacobian
    A = zeros(2);
    A1 = zeros(2);
    A2 = zeros(2);

    % Generate the grid
    nSteps = abs(model.gridSize/model.stepSize);
    mu = zeros(nSteps);

    RA_Lens1 = model.RA_Lens1;
    Dec_Lens1 = model.Dec_Lens1;
    RA_Lens2 = model.RA_Lens2;
```

```
    Dec_Lens2 = model.Dec_Lens2;

    % Find the coordinate (x1Start,x2Start) of the top left cell in the grid
    % The starting position is defined from the mid-point on the line joining the two
point masses
    RA_Center = RA_Lens1 - ((RA_Lens1 - RA_Lens2)/2);
    Dec_Center = Dec_Lens1 - ((Dec_Lens1 - Dec_Lens2)/2);

    x1Start = RA_Center + abs(model.gridSize/2);
    x2Start = Dec_Center + abs(model.gridSize/2);

    string = sprintf('\nLens 1 = (%f,%f)\nLens2 = (%f,%f)\nOrigin = (%f,%f)\nStart point
= (%f,%f)\nNo. of steps = %d\n',RA_Lens1, Dec_Lens1, RA_Lens2, Dec_Lens2, RA_Center,
Dec_Center, x1Start, x2Start,nSteps);
    disp(string);

    disp('Generating the magnification map');

    % Process the grid for lens1
    x2This = x2Start; % x2 coordinate of the current cell
    for i=1:nSteps
        x1This = x1Start; % x1 coordinate of the current cell
        for j=1:nSteps

            % Compute surface mass density for this point (x1,x2)
            surfDensity = model.M_lens * Delta(x1This-RA_Lens1,x2This-Dec_Lens1);

            % Compute convergence for this point
            kappa = surfDensity / critDensity;

            % Find distance between this point and the lens
            x1 = RA_Lens1 - x1This;
            x2 = Dec_Lens1 - x2This;
            x = sqrt(x1^2 + x2^2);

            % Compute the first matrix in A
            norm1 = (1/(x^4));
            Mat1(1,1) = norm1*((x2^2) - (x1^2));
            Mat1(1,2) = norm1*(-2*x1*x2);
            Mat1(2,1) = Mat1(1,2);
            Mat1(2,2) = norm1*((x1^2) - (x2^2));

            % Compute the second matrix in A
            norm2 = (2*x*kappa) / (x^3);
            Mat2(1,1) = norm2 * (x1^2);
            Mat2(1,2) = norm2 * x1 * x2;
            Mat2(2,1) = Mat2(1,2);
            Mat2(2,2) = norm2 * (x2^2);

            A1 = I_2D-Mat1-Mat2;

            % Clear the required variables in order to compute A of the second lens
            clear surfDensity kappa x1 x2 x norm1 Mat1 norm2 Mat2;

            % Start computing the Jacobian matrix for Lens 2
            % Compute surface mass density for this point (x1,x2)
            surfDensity = model.M_lens * Delta(x1This-RA_Lens2,x2This-Dec_Lens2);
```

```
            % Compute convergence for this point
            kappa = surfDensity / critDensity;

            % Find distance between this point and the lens
            x1 = RA_Lens2 - x1This;
            x2 = Dec_Lens2 - x2This;
            x = sqrt(x1^2 + x2^2);

            % Compute the first matrix in A
            norm1 = (1/(x^4));
            Mat1(1,1) = norm1*((x2^2) - (x1^2));
            Mat1(1,2) = norm1*(-2*x1*x2);
            Mat1(2,1) = Mat1(1,2);
            Mat1(2,2) = norm1*((x1^2) - (x2^2));

            % Compute the second matrix in A
            norm2 = (2*x*kappa) / (x^3);
            Mat2(1,1) = norm2 * (x1^2);
            Mat2(1,2) = norm2 * x1 * x2;
            Mat2(2,1) = Mat2(1,2);
            Mat2(2,2) = norm2 * (x2^2);

            % Jacobian Matrix for Lens 2
            A2 = I_2D-Mat1-Mat2;

            % Add both the Jacobian matrices
            A = A1 + A2;

            % Compute mu for this point
            %mu(i,j) = abs(1 / ((A(1,1)*A(2,2)) - (A(2,1)*A(1,2))));
            mu(i,j) = (1 / ((A(1,1)*A(2,2)) - (A(2,1)*A(1,2))));

            % Decrement x1This per j loop as RA decreases towards the right
            x1This = x1This - model.stepSize;
        end
        % Decrement x2This per i loop as Dec decreases downwards
        x2This = x2This - model.stepSize;
    end

    % Plot the magnification matrix
    pcolor(mu);
    shading('interp');
    colorbar;
    caxis([-2 2])
end
```

```
% ------------------------------------------------------------
%
% Input parameters for the lens model
%
% ------------------------------------------------------------

function y = modelParam()

    % Redshift of the lens
    z_lens = 0.46;

    % Redshift of the source
    z_source = 2.15;

    % Mass of the lens [solar mass]
    M_lens = 1.25E9;
        M_lens = M_lens * 1.99E30;

    % Specify the size of the grid [arcsec]
    gridSize = 4;

    % Step size [arcsec] - Angular separation between neighbouring grid cells
    stepSize = 0.005;

    % RA and dec of Lens 1 [arcsec]
    RA_Lens1 = 2.0; % 2.05
    Dec_Lens1 = 0;

    % RA and dec of Lens 2 [arcsec]
    RA_Lens2 = 0;
    Dec_Lens2 = 0;

    %%% DO NOT MODIFY BELOW THIS LINE %%%
    y = struct('z_lens',z_lens,'z_source',z_source,'M_lens',M_lens,'gridSize',↙
gridSize,'stepSize',stepSize,'RA_Lens1',RA_Lens1,'Dec_Lens1',Dec_Lens1,'RA_Lens2',↙
RA_Lens2,'Dec_Lens2',Dec_Lens2);
```

```
% ------------------------------------------------------------------------
%
% Cosmological model
%
% ------------------------------------------------------------------------

function y = cosmoParam()
    % Energy density of dark energy
    Om_lambda = 0.728;

    % Energy density of baryonic and non-baryonic matter
    Om_m = 0.272;

    % Energy density due to spatial curvature
    Om_k = 0;

    % Hubble constant [km/s/Mpc]
    H_0 = 70.2;
        H_0 = H_0/(3.08E19);

    % Velocity of light [m/s]
    c = 299792458;

    % Gravitational constant
    G = 6.673E-11;

    %%% DO NOT EDIT BEYOND THIS LINE %%%
    y = struct('Om_lambda',Om_lambda,'Om_m',Om_m,'Om_k',Om_k,'H_0',H_0,'c',c,'G',G);
```

```
% ------------------------------------------------------------------
%
% Compute the LoS co-moving distance to the specified redshift
%
% ------------------------------------------------------------------

function y = getCoMovDist(z)
    cosmo = cosmoParam();

    X = 0:z/50:z;
    fun = 1./sqrt(((cosmo.Om_m.*((1+X).^3))) + cosmo.Om_lambda + (cosmo.Om_k.*((1+X).↙
^2)));
    Integ = trapz(X,fun);

    y = (cosmo.c/cosmo.H_0)*Integ;

    % Convert [y] from [m] to [Mpc]
    y = y/(3.09E22);
end

% ------------------------------------------------------------------
%
% Dirac Delta function
%
% ------------------------------------------------------------------

function y = Delta(A,B)

    if ((A == 0) & (B == 0))
        y = 1;
    else
        y = 0;
    end
end

% ------------------------------------------------------------------
%
% Code to check the validity of the lens model parameters
%   defined in modelParam.m
%
% ------------------------------------------------------------------

function y = checkModel()

    model = modelParam();

    if model.z_lens>=model.z_source
        y = 1;
    elseif model.M_lens < 0
        y = 1;
    else
        y = 0;
    end
end
```

Appendix H

Magnification map for a double SIS lens

The MATLAB code used to generate the magnification maps for a double SIS lens is presented in this appendix. The lens model and the cosmological model are defined in functions *modelParam* and *cosmoParam* respectively. The main code is written in the file *Code.m*. This MATLAB code can be extended to generate magnification maps for any canonical mass distribution with very little modification to the code in the file *Code.m*. Note that in the current version of the code, both SIS lenses are assumed to be at the same redshift.

```
% ------------------------------------------------------------------------
%
%   Code to generate magnification maps for a 2-SIS lens
%
%   Based on Shin & Evans (2008)
%
% ------------------------------------------------------------------------

clear all;

model = modelParam();
cosmo = cosmoParam();

% Scale all distances by 1 Kpc
scale = 1; % [Kpc]
% ------------------------------------------------------------------------
% Check for the validity of the input parameters
% ------------------------------------------------------------------------
flag = checkModel();

if flag == 1
    disp('Incorrect model parameters. Execution terminated!!!');
else
    disp('Input parameters verified. Proceeding to build the model');

% ------------------------------------------------------------------------
% Compute the required cosmological distances
% ------------------------------------------------------------------------
    disp('Computing the cosmological distances');
    %   Observer-to-lens
    D_d = getCoMovDist(model.z_lens)/(1+model.z_lens);

    %   Observer-to-source
    D_s = getCoMovDist(model.z_source)/(1+model.z_source);

    %   lens-to-source
    D_ds = (getCoMovDist(model.z_source) - getCoMovDist(model.z_lens))/(1+model.↙
z_source);

    % Compute the Einstein radii for both the spheres - Both spheres are at the same↙
redshift
    E_1 = 4 * pi * ((model.velDisp_1/cosmo.c)^2) * ((D_d*D_ds)/D_s);
    E_2 = 4 * pi * ((model.velDisp_2/cosmo.c)^2) * ((D_d*D_ds)/D_s);

    % Write Einstein radii in dimensionless units by scaling with 1 Kpc
    E_1 = (E_1 * 1000)/scale;
    E_2 = (E_2 * 1000)/scale;

    % Convert the specified grid size to scaled units
    scaledGridSize = (model.gridSize/206264.81) * D_d * 1E3;

    % Convert the step size to scaled units
    scaledStepSize = (model.stepSize/206264.81) * D_d * 1E3;

    % Convert the core radii to dimensionless units
    R_core_1 = model.R_core_1 / 1000;
    R_core_2 = model.R_core_2 / 1000;
```

```
    % Find the coordinate of the top left cell in the grid
    xStart = -scaledGridSize/2;
    yStart = scaledGridSize/2;

    % No. of steps
    nSteps = abs(scaledGridSize/scaledStepSize);

    mu = zeros(nSteps);

    y = yStart;
    for i = 1:nSteps
        x = xStart;
        for j = 1:nSteps

            % Compute r1 and r2 as defined in Shin & Evans (2008)
            r1_squared = (model.a + x)^2 + y^2;
            r2_squared = (model.a - x)^2 + y^2;

            % Shear at each point
            gamma_1 = ((E_1/2)*((y^2)-(model.a+x)^2)/power((R_core_1^2 + r1_squared),↙
3/2)) + ((E_2/2)*((y^2)-(model.a-x)^2)/power((R_core_2^2 + r2_squared),3/2));
            gamma_2 = (E_2 * y * (model.a - x))/power((R_core_2^2 + r2_squared),3/2) -↙
(E_1 * y * (model.a + x))/power((R_core_1^2 + r1_squared),3/2);

            gamma = sqrt(gamma_1^2 + gamma_2^2);

            % Compute kappa at each point
            kappa = ((E_1/2) * (2*(R_core_1^2)+r1_squared)/power(R_core_1^2 +↙
r1_squared,3/2)) + ((E_2/2) * (2*(R_core_2^2)+r2_squared)/power(R_core_2^2 + r2_squared,↙
3/2));

            % Determinant of the magnification matrix
            detA = (1-kappa)^2 - gamma^2;

            %mu(i,j) = abs(1/detA);
            mu(i,j) = 1/detA;

            % Decrement x per loop
            x = x + scaledStepSize;
        end
        % Decrement y per loop
        y = y - scaledStepSize;
    end

    % Plot the magnification matrix
    pcolor(mu);
    shading('interp');
    colormap('jet');
    colorbar;
    title('Magnification map');
    caxis([-64 64]);

end
```

```
% ------------------------------------------------------------------------
%
% Input parameters for the lens model
%
% ------------------------------------------------------------------------

function y = modelParam()

    % Redshift of the lens
    z_lens = 0.46;

    % Redshift of the source
    z_source = 2.15;

    % Specify the size of the grid [arcsec]
    gridSize = 8;

    % Step size [arcsec] - Angular separation in arcsec between two neighboring grid↙
cells
    stepSize = 0.01;

    % Core radius for both the sphere [pc]
    R_core_1 = 100;
    R_core_2 = 100;

    % Rotational velocities of stars in both the galaxies [km/s]
    velDisp_1 = 200;
    velDisp_2 = 200;
        velDisp_1 = velDisp_1 * 1000; % [m/s]
        velDisp_2 = velDisp_2 * 1000; % [m/s]

    % Separation between the two spheres - use same units as in Shin & Evans (2008)
    a = 4;

    %%% DO NOT EDIT BELOW THIS LINE %%%
    y = struct('z_lens',z_lens, 'z_source',z_source, 'gridSize',gridSize, 'stepSize',↙
stepSize, 'R_core_1',R_core_1, 'R_core_2',R_core_2, 'velDisp_1',velDisp_1, 'velDisp_2',↙
velDisp_2, 'a',a);
```

```
% ------------------------------------------------------------------------
%
% Cosmological parameters and physical constants
%
% ------------------------------------------------------------------------

function y = cosmoParam()
    % Energy density of dark energy
    Om_lambda = 0.728;

    % Energy density of baryonic and non-baryonic matter
    Om_m = 0.272;

    % Energy density due to spatial curvature
    Om_k = 0;

    % Hubble constant [km/s/Mpc]
    H_0 = 70.2;
        H_0 = H_0/(3.08E19);

    % Velocity of light [m/s]
    c = 299792458;

    % Gravitational constant
    G = 6.673E-11;

    y = struct('Om_lambda',Om_lambda,'Om_m',Om_m,'Om_k',Om_k,'H_0',H_0,'c',c,'G',G);
```

```
% ------------------------------------------------------------------------
%
% Compute the LoS co-moving distance to the specified redshift
%
% ------------------------------------------------------------------------

function y = getCoMovDist(z)
    cosmo = cosmoParam();

    X = 0:z/50:z;
    fun = 1./sqrt(((cosmo.Om_m.*((1+X).^3))) + cosmo.Om_lambda + (cosmo.Om_k.*((1+X).↙
^2)));
    Integ = trapz(X,fun);

    y = (cosmo.c/cosmo.H_0)*Integ;

    % Convert [y] from meter to Mpc
    y = y/(3.09E22);
end

% ------------------------------------------------------------------------
%
% Dirac Delta function
%
% ------------------------------------------------------------------------

function y = Delta(A,B)

    if ((A == 0) & (B == 0))
        y = 1;
    else
        y = 0;
    end
end

% ------------------------------------------------------------------------
%
% Code to check the validity of the lens model parameters defined in modelParam.m
%
% ------------------------------------------------------------------------

function y = checkModel()

    model = modelParam();

    if model.z_lens>=model.z_source
        y = 1;
    elseif (model.velDisp_1 < 0 | model.velDisp_2 < 0)
        y = 1;
    else
        y = 0;
    end
end
```